Hygroscopic behavior of NaCl–MgCl₂ mixture particles as nascent sea-spray aerosol surrogates and observation of efflorescence during humidification

D. Gupta[+], H.-J. Eom[+], H.-R. Cho, and C.-U. Ro[*]

Department of Chemistry, Inha University, Incheon, 402-751, Korea

ABSTRACT

As Na^+, Mg^{2+}, and Cl^- are major ionic constituents of seawater, NaCl–MgCl₂ mixture particles might represent sea-spray aerosols (SSAs) better than pure NaCl. However, there have been very few hygroscopic studies of pure MgCl₂ and NaCl–MgCl₂ mixture aerosol particles despite the MgCl₂ moiety playing a major role in the hygroscopic behavior of nascent SSAs. Laboratory-generated pure MgCl₂ and NaCl–MgCl₂ mixture aerosol particles with 12 mixing ratios ($0.01 \leq$ mole fraction of NaCl (X_{NaCl}) ≤ 0.9) were examined systematically by optical microscopy (OM), in-situ Raman microspectrometry (RMS), and scanning electron microscopy/energy dispersive X-ray spectrometry (SEM/EDX) elemental X-ray mapping to observe their hygroscopic behavior, derive the experimental phase diagrams, and obtain the chemical micro-structures. Dry-deposited $MgCl_2 \cdot 6H_2O$ particles exhibited a deliquescence relative humidity (DRH) of ~ 33.0 % and an efflorescence RH (ERH) of 10.8–9.1 %, whereas the nebulized pure MgCl₂ and MgCl₂-dominant particles of $X_{NaCl} = 0.026$ (eutonic) and 0.01 showed single-stage transitions at DRH of ~ 15.9 % and ERH of 10.1–3.2 %. The characteristic OH-stretching Raman signatures indicated the crystallization of $MgCl_2 \cdot 4H_2O$ at low RHs, suggesting that the kinetic barrier to $MgCl_2 \cdot 6H_2O$ crystallization is not overcome in the timescale of the dehydration measurements. The NaCl–MgCl₂ mixture particles of $0.05 \leq X_{NaCl} \leq 0.9$ generally showed two-stage deliquescence: first at the mutual DRH (MDRH) of ~15.9 %; and second with the complete dissolution of NaCl at the second DRHs depending on the mixing ratios, resulting in a phase diagram composed of three distinct phases. During dehydration, most particles of $0.05 \leq X_{NaCl} \leq 0.9$ exhibited two-stage efflorescence: first, by the homogeneous

+ Authors with equal contributions

[*]Corresponding author. Tel: +82 32 860 7676; fax: +82 32 867 5604; E-mail address: curo@inha.ac.kr

28   nucleation of NaCl; and second, at mutual ERH (MERH) of ~ 10.4–2.9 %, by the crystallization

29   of the $MgCl_2 \cdot 4H_2O$ moiety, also resulting in three distinct phases. Interestingly, particles of X_{NaCl}

30   = 0.1 and 0.2 frequently showed 3 different types of mutual deliquescence behaviors. The first

31   type exhibited an MDRH at ~15.9 %. The second exhibited the first MDRH at ~15.9 %,

32   efflorescence to $MgCl_2 \cdot 6H_2O$ (confirmed by in-situ RMS) at RH of ~16.1–25.0 %, and a second

33   MDRH at ~33.0 %. The third showed an MDRH at ~33.0 %. Some particles of $X_{NaCl} = 0.1$ and

34   0.2 also exhibited higher MERHs = 15.2–11.9 % and 23.7–15.3 %, respectively, forming

35   $MgCl_2 \cdot 6H_2O$. These observations suggest that the presence of sufficient condensed water and

36   optimally sized crystalline NaCl (X_{NaCl} = 0.1 and 0.2) acting as heterogeneous nucleation seeds

37   helps overcome the kinetic barrier, leading to the structural growth and crystallization of

38   $MgCl_2 \cdot 6H_2O$. SEM/EDX elemental X-ray mapping showed that the effloresced NaCl-rich

39   particles contain homogeneously crystallized NaCl in the center, surrounded by $MgCl_2 \cdot 4H_2O$.

40   The observation of an aqueous phase over a wider RH range for NaCl–$MgCl_2$ mixture particles

41   indicates their more probable heterogeneous chemistry compared to pure NaCl particles as a

42   nascent SSA surrogate.

43

44   **INTRODUCTION**

45   Sea-salt or sea-spray aerosols (SSAs) are produced from waves through bubble bursting

46   and constitute the second most abundant natural atmospheric aerosols (25-50% of the aerosol

47   mass) after mineral dust particles (Finlayson-Pitts and Pitts, 2000). A study of the hygroscopic

48   behavior of inorganic aerosol particles, closely simulating the chemical compositions of nascent

49   sea-salts, should provide valuable insights into several important SSA properties: (i)

50   aerodynamic properties, (ii) cloud-droplet nucleation efficiency, (iii) optical properties, and (iv)

51   physicochemical changes through complicated heterogeneous chemical reactions with various

52   atmospheric gas-phase species (Meskhidze et al., 2013; King et al., 2012; Tang et al., 1997;

53   Haywood and Boucher, 2000; ten Brink, 1998; Krueger et al., 2003). For nascent SSAs, the

54   major ionic constituents are Cl^-, Na^+, SO_4^{2-}, Mg^{2+}, Ca^{2+}, and K^+ (Seinfeld and Pandis, 2006).

55   Because NaCl constitutes ~ 80 % of sea-salts by mass, it has long been treated as a nascent SSA

56   surrogate, i.e., the hygroscopic behavior of a single-component NaCl aerosol system has been

57   used to parametrize the thermodynamic and optical properties and cloud activation efficiency of

58   nascent ambient SSAs (Tang et al., 1997; Niedermeier et al., 2008). On the other hand, nascent
59   SSAs can react with gaseous species, such as NO_x and HNO_3/H_2SO_4, within few minutes to
60   hours of their residence in air (ten Brink, 1998; Saul et al., 2006; Liu et al., 2007). Further, these
61   partially or fully reacted SSAs can interact with volatile organic carbons (VOCs), secondary
62   organic aerosols (SOAs), etc. Previous studies have been performed to explore the hygroscopic
63   properties of these aged SSAs. For example, the hygroscopic behavior of laboratory generated
64   aerosol particles of NaCl mixed with dicarboxylic acids (stable water-soluble organics) was
65   reported (Krieger et al., 2012; Ghorai et al., 2014; Ma et al., 2013). In addition, it was
66   demonstrated that both airborne and laboratory-generated SSAs are complicated in their
67   chemical characteristics and mixing states (Wise et al., 2007; Wise et al., 2009; Prather et al.,
68   2013). Therefore, the current understanding of the hygroscopic properties of ambient SSAs is
69   "low" as reported in a recent review by Meskhidze et al. (2013). The contributions from other
70   constituents, such as sea-salt (ss)-SO_4^{2-}, non-sea-salt (nss)-SO_4^{2-}, NO_3^-, and organics cannot be
71   evaluated further unless the hygroscopic behavior of the primary inorganics in nascent SSAs is
72   clearly defined.

73         $MgCl_2$, the second most abundant constituent of nascent SSAs, plays a key role in
74   heterogeneous atmospheric chemistry as well as chemical fractionation in ambient or laboratory-
75   generated SSAs. For example, the uptake of gaseous HNO_3 was claimed to be faster on the
76   NaCl−$MgCl_2$ mixture particles than on the pure NaCl particles (Saul et al., 2006; Liu et al.,
77   2007); Mg^{2+} and organic species mainly constituted the submicron SSAs generated from a
78   laboratory ocean-atmosphere facility, whereas NaCl dominated the supermicron inorganic SSAs
79   (Prather et al., 2013); in marine aerosols, a Mg^{2+}–rich chloride moiety was segregated from the
80   NaCl moiety (Wise et al., 2007; Gaston et al., 2011); and the SSAs collected at an Antarctic
81   coastal site (Hara et al., 2012) and during the JASE traverse campaign (Hara et al., 2014) were
82   fractionated into Mg-rich and NaCl-rich salt particles. In addition, it was reported that
83   laboratory-generated SSAs and pure $MgCl_2$ contained residual water, even at very low relative
84   humidity (RH) (Cziczo et al., 1997; Cziczo and Abbatt, 2000; Tang et al., 1997). The
85   hygroscopic growth factors of ambient or laboratory-generated SSAs plotted as a function of the
86   RH were reported to be different from that of pure NaCl (Tang et al., 1997; Ahn et al., 2010;
87   Schindelholz et al., 2014). This different hygroscopic behavior can affect the cloud droplet

88   nucleation efficiency. For example, the critical supersaturation for the cloud droplet nucleation of

89   particles generated from an artificial seawater−oxalic acid mixture was closer to that of

90   NaCl−MgCl$_2$−oxalic acid mixture particles than that of NaCl−oxalic acid mixture (Drozd et al.,

91   2014). Therefore, NaCl−MgCl$_2$ mixture particles might better represent the hygroscopic behavior

92   of nascent SSAs.

93   To obtain a better understanding for hygroscopic behavior of the NaCl−MgCl$_2$ mixture

94   particles, the hygroscopic properties of pure NaCl and MgCl$_2$ salts need to be understood first.

95   The hygroscopic properties of pure NaCl particles are well established. Briefly, during the

96   humidification process, where RH is changed from low to high, solid NaCl particles at low RH

97   dissolve completely and form aqueous droplets at the deliquescence RH (DRH) of ~ 75 %.

98   During the dehydration process, where RH is changed from high to low, the concentration of

99   NaCl in the aqueous droplets becomes dense as the RH is decreased and NaCl finally crystallizes

100   at its efflorescence RH (ERH) of ~ 45−47 %, which is significantly lower than its DRH (Martin,

101   2000).

102   However, there have been few hygroscopic studies of pure MgCl$_2$ aerosol particles, even

103   though the MgCl$_2$ moiety plays a major role in the hygroscopic behavior of nascent SSAs.

104   MgCl$_2$·6H$_2$O is the most thermodynamically stable hydrate of bulk MgCl$_2$ crystals with a DRH

105   of 33 % at room temperature (Lide, 2002). Thus far, only two experiments reported a DRH of

106   ~33 % for aerosol particles nebulized from a MgCl$_2$·6H$_2$O aqueous solution (Ha and Chan, 1999;

107   Park et al., 2009). On the other hand, in a flow tube FTIR measurement, it was reported that dry

108   MgCl$_2$ particles began to uptake water at RHs << 33%, even though the DRH values were not

109   clearly defined (Cziczo and Abbatt, 2000). Furthermore, just one experiment reported ERH of 14

110   (±4) % (T = 243 K) for MgCl$_2$ aerosol particles (Gough et al., 2014). Therefore, the hygroscopic

111   behavior of pure MgCl$_2$ aerosol particles was examined systematically in this work for the first

112   time.

113   To the best of the authors' knowledge, there has been no systematic experimental work on

114   the hygroscopic behavior of binary NaCl−MgCl$_2$ mixture particles. In the only report thus far, for

115   an equimolar mixing ratio of NaCl and MgCl$_2$, Chan et al. (2000) observed the first ERH at 38 %

116   and calculated a mutual DRH (MDRH) of 32 % and a second DRH of 70 % based on the bulk

117   NaCl−MgCl$_2$−H$_2$O system phase diagram (Seidell and Linke, 1965).

118   In the present study, the hygroscopic behavior, physical states/phases, and
119   microstructures of pure $MgCl_2$ and $NaCl–MgCl_2$ mixture particles (covering twelve mixing
120   ratios with NaCl mole fractions ranging from 0.01 to 0.9) were examined by optical microscopy
121   (OM), in-situ Raman microspectrometry (RMS), and scanning electron microscopy/energy
122   dispersive X-ray spectrometry (SEM/EDX). The phase transitions of the micrometer sized,
123   laboratory-generated aerosol particles at room temperature were observed by monitoring the size
124   change of the particles in the optical images as a function of the RH. The experimentally
125   measured MDRHs and DRHs were compared with those derived theoretically from the Aerosol
126   Inorganic-Organic Mixtures Functional group Activity Coefficients (AIOMFAC) model
127   calculations (http://www.aiomfac.caltech.edu) (Zuend et al., 2008; Zuend et al., 2011). In-situ
128   RMS was used to observe the phase/structural changes to complement the measurements by OM.
129   SEM/EDX elemental X-ray mapping was used to examine the compositional distribution in
130   effloresced particles. This study systematically describes the full hygroscopic behavior of
131    $NaCl–MgCl_2$ binary aerosol particles at twelve different mixing ratios.

132

2. EXPERIMENTAL SECTION

2.1 Preparation of NaCl-MgCl₂ mixture particles

135   Mixed $NaCl–MgCl_2$ particles were generated by the nebulization of aqueous solutions
136   with different $NaCl:MgCl_2$ mixing ratios. Pure solutions (1.0 M each) of NaCl and $MgCl_2 \cdot 6H_2O$
137   (NaCl, > 99.9% purity, Aldrich; $MgCl_2 \cdot 6H_2O$, 99.9% purity, Aldrich) were prepared, and
138   solutions with 12 different mixing ratios were made by mixing the two solutions volumetrically.
139   A single jet atomizer (HCT4810) was used to generate the aerosol particles to be deposited on
140   the substrates. For all OM observations and most in-situ RMS measurements, the substrate used
141   was Parafilm-M, which is a hydrophobic substrate with a contact angle of 106.8° ± 0.4° for de-
142   ionized water droplets (Eom et al., 2014). Pure NaCl particles were wet-deposited on the
143   Parafilm-M substrates and their hygroscopic properties were measured to check the accuracy of
144   the experimental set-up. A dry powder or nebulized pure $MgCl_2 \cdot 6H_2O$ particles and some
145    $NaCl–MgCl_2$ mixture particles were deposited on a TEM grid and/or Al substrates to perform
146   off-line SEM/EDX measurements after the hygroscopic measurements by OM to avoid charging

147   by the electron-beam on the Parafilm-M substrates. The size of the dry- and wet-deposited

148   particles ranged from 1 to 10 μm.

149   NaCl−MgCl$_2$ mixture particles with 12 different mixing ratios were investigated, i.e., 11

150   compositions with NaCl mole fractions of 0.01−0.9 (X_{NaCl} = 0.01, 0.05, 0.1, 0.2, 0.3, 0.4, 0.5, 0.6,

151   0.7, 0.8, and 0.9, where X_{NaCl} represents the mole fraction of NaCl.) and a eutonic composition

152   (X_{NaCl} = 0.026, which was calculated from the ionic activity products predicted by the AIOMFAC

153   model). Unlike the eutonic compositions of other binary mixture particles, such as NaCl−KCl

154   (X_{NaCl} = 0.7) (Li et al., 2014) and NaCl−NaNO$_3$ (X_{NaCl} = 0.38) (Gupta et al., 2015), the

155   NaCl−MgCl$_2$ mixture system has a MgCl$_2$-dominant eutonic composition. In the context of

156   thermodynamics, particles with a composition of X_{NaCl} > 0.026 were defined as NaCl-rich and

157   those with X_{NaCl} < 0.026 were defined as MgCl$_2$-rich.

158   2.2 Hygroscopic property measurement

159   2.2.1 Optical microscopy (OM)

160   The hygroscopic properties of the particles were investigated using a "see-through"

161   inertia impactor apparatus equipped with an optical microscope. The experimental set-up is

162   described in detail elsewhere (Ahn et al., 2010). Briefly, the apparatus was composed of three

163   parts: (A) see-through impactor, (B) optical microscope and (C) humidity controlling system.

164   The Parafilm-M substrate onto which the aerosol particles were deposited was mounted on the

165   impaction plate in the see-through impactor. The RH inside the impactor was controlled by

166   mixing dry and wet (saturated with water vapor) N$_2$ gases. The wet N$_2$ gas was obtained by

167   bubbling through two deionized water reservoirs. The flow rates of the dry and wet N$_2$ gases

168   were controlled by mass flow controllers to obtain the desired RH in the range of ~3−90 %,

169   which was monitored by a digital hygrometer (Testo 645). The digital hygrometer was calibrated

170   using a dew-point hygrometer (M2 Plus-RH, GE), providing RH readings of ± 0.5 %

171   reproducibility. The particles on the impaction plate were observed through a nozzle throat using

172   an optical microscope (Olympus, BX51M) equipped with 50x/0.5 numerical aperture objective.

173   The images of particles were recorded by a digital camera (Canon EOS 5D, full frame, Canon EF

174   f/3.5 L macro USM lens) during the humidification (by increasing RH from ~ 3 to 90 %) and

175   dehydration (by decreasing RH from ~ 90 to 3 %) experiments. The image size was 5616 × 3744

176 pixels and the image recording condition was set according to the ISO500. The exposure time

177 was 0.4 s and the depth of focus (DOF) was F/3.5. All the hygroscopic experiments were carried

178 out at room temperature (T = 23 ± 1 $^{\circ}$C).

179 The changes in particle size with the variation of RH was monitored by measuring the

180 particle areas in the optical images (Ahn et al., 2010). The particle images were processed using

181 image analysis software (Matrox, Inspector v9.0). The size of the imaging pixel was calibrated

182 using 10 μm Olympus scale bars. Although particles larger than 0.5 μm in 2D diameter (D_p)

183 could be analyzed using this system, image fields with particles of 1−10 μm were selected

184 because high quality hygroscopic OM data can be obtained from them. Each humidity condition

185 was sustained for at least 2 min. A steady state (or quasi-equilibrium) is reached in much shorter

186 time than 2 min which can be clearly confirmed by the sudden morphological and/or size change

187 of particles/droplets responding to the RH change and no further morphological and/or size

188 change thereafter. Just to make sure the equilibrium state is attained after the RH change, the

189 optical image of an "ensemble of particles" was recorded after 2 min from each step of RH

190 change.

191 **2.2.2 In-situ Raman microspectrometry (RMS)**

192 In-situ RMS measurements were carried out under controlled RHs to observe the

193 structural changes in the hydrated water in $MgCl_2$ crystalline solids. The apparatus is composed

194 of three parts: (A) see-through impactor, (B) Raman microscope/spectrometer and (C) humidity

195 controlling system. The experimental set-up is similar to that used for optical microscopy, with

196 the Raman spectrometer replacing the optical microscope, i.e., the particle impaction and RH

197 controlling system are precisely the same as for the standalone optical microscopy system. The

198 RH was monitored using a digital hygrometer (Testo 635). The digital hygrometer was calibrated

199 using a dew-point hygrometer (M2 Plus-RH, GE), providing RH readings with ±1.5 %

200 reproducibility. The in-situ Raman spectra of the particles deposited on Parafilm-M or Al

201 substrates were recorded using a confocal Raman microspectrometer (XploRA, Horiba Jobin

202 Yvon) equipped with a 50x/0.5 numerical aperture objective (Olympus). The optical image size

203 was 908 × 680 pixels. An excitation laser with a wavelength of 532 nm and 3 mW power was

204 used and the scattered Raman signals were detected using an air cooled multichannel charge-

205   coupled device (CCD) detector. The data acquisition time was 10 s for each measurement. The

206   spectral resolution was 1.8 cm^{-1}. The spectra and images were acquired and processed using

207   Labspec6 software.

208   OM images have a higher spatial resolution (5616 × 3744 pixels) than the RMS optical

209   images (908 × 680 pixels), so that they can be processed more accurately for monitoring the 2D

210   size changes and the two measurements were performed separately. Unlike the closely monitored

211   OM images, which were recorded in RH steps of ~0.3 % to generate the 2D area growth curves

212   (Ahn et al., 2010), the Raman spectra of the individual particles were recorded in RH steps of

213   ~3.0 % (~10 min. for an ensemble of particles at each RH) to detect the phase changes and

214   complement the OM data.

215   **2.3. SEM/EDX elemental X-ray mapping of effloresced particles**

216   After the hygroscopicity measurements of the individual particles, SEM/EDX was

217   performed on the effloresced NaCl−$MgCl_2$ mixture particles to determine the morphology and

218   spatial distribution of the chemical elements (Li et al., 2014; Gupta et al., 2015). The SEM/EDX

219   measurements were carried out using a Jeol JSM-6390 SEM equipped with an Oxford Link

220   SATW ultrathin window EDX detector. The resolution of the detector was 133 eV for Mn Kα X-

221   rays. The X-ray spectra and elemental X-ray maps were recorded using Oxford INCA Energy

222   software. A 10 kV accelerating voltage and 0.5 nA beam current was used and the typical

223   measuring times for elemental X-ray mapping were 5 min.

224

225   **3. RESULTS AND DISCUSSION**

226   **3.1 Hygroscopic behavior of pure NaCl and $MgCl_2$ particles**

227   Figure 1 shows the 2-D area ratio plots as a function of the RH for the representative wet-

228   deposited NaCl and $MgCl_2$ particles. The humidification and dehydration curves are represented

229   as the area ratio (A/A_0: left-hand axis), where the 2-D projected particle area at a given RH (A) is

230   divided by that before starting the humidification process (A_0).

8

231   As shown in Fig. 1a, all 26 wet-deposited aerosol particles on an optical image field,

232   which were generated by nebulization from a pure NaCl aqueous solution, showed typical

233   hysteresis curves with DRH of 75.1 ($\pm$0.5) % and ERH of 47.6 $-$ 45.7 %, and these values are

234   consistent with the reported values (Tang et al., 1997; Wise et al., 2007) and previous results

235   (Ahn et al., 2010; Eom et al., 2014).

236   All 30 wet-deposited aerosol particles nebulized from an 1 M $MgCl_2 \cdot 6H_2O$ aqueous

237   solution showed a prompt deliquescence transition at DRH of 15.9 ($\pm$0.3) % and a distinct

238   efflorescence transition in the RH range of 10.1 $-$ 3.2 % with a mean ERH of 5.9 % (Fig. 1b). At

239   room temperature, thermodynamically stable bulk solids are in the form of $MgCl_2 \cdot 6H_2O$, which

240   was reported to have a DRH of ~33.0 % (Lide, 2002). On the other hand, the AIOMFAC model

241   predicts its DRH as 36.7 %, which is somewhat biased on the higher side. Until now, just two

242   experiments reported the DRH as ~ 33.0 %, which is similar to the thermodynamic bulk DRH of

243    $MgCl_2 \cdot 6H_2O$, for aerosol particles nebulized from an $MgCl_2 \cdot 6H_2O$ aqueous solution despite no

244   ERHs being obtained (Ha and Chan, 1999; Park et al., 2009). On the other hand, in a flow tube

245   FTIR measurement, it was reported that the dry $MgCl_2$ particles began to uptake water at much

246   lower RHs than 33%, which is similar to the current results, even though the DRH values were

247   not defined (Cziczo and Abbatt, 2000). In addition, they suggested the presence of an $MgCl_2$

248   hydrate crystal at RH of < 2%. Until now, no ERH for $MgCl_2$ aerosol particles has been reported,

249   with the exception of one at T = 243 K, which was 14 ($\pm$4) % (Gough et al., 2014).

250   As the observation of a distinct DRH and ERH indicated the presence of a crystalline

251    $MgCl_2$ hydrate after efflorescence, in-situ RMS measurements of dry-deposited (powdery) and

252   nebulized $MgCl_2 \cdot 6H_2O$ particles were performed to identify the crystal form of the hydrates.

253   Figure 2 shows optical images and corresponding Raman spectra for a dry-deposited and a

254   nebulized $MgCl_2 \cdot 6H_2O$ particles, which were recorded during the in-situ RMS measurements.

255   During the humidification process, the irregular-shaped powder particle existed as crystalline

256    $MgCl_2 \cdot 6H_2O$ until RH = 30.6 %, as confirmed by its typical Raman OH stretching signatures

257   (ν(OH) = ~3350, 3390, and 3510 cm^{-1}) (Fig. 2a) (Musick et al., 1999; Gough et al., 2014). At RH

258   = 34.7%, the powder particle became a round droplet and the OH vibration signal for free water

259   (ν(OH) = ~3420 cm^{-1}) was observed, indicating that the deliquescence transition had occurred in

260   the RH range of 30.6 $-$ 34.7 %, which is typical for $MgCl_2 \cdot 6H_2O$ solids (DRH = 33 %). During

261   the dehydration process (Fig. 2b), the aqueous $MgCl_2$ droplet kept showing a broad free water

262   Raman signal until RH = 15.7 %. At RH = 10.8 %, the optical image showed a morphological

263   change (despite the particle remaining in a round shape), and new OH vibration signals ($\nu(OH)$ =

264   ~3405 and ~3440 cm^{-1}) typical for $MgCl_2 \cdot 4H_2O$ (Gough et al., 2014) were observed, indicating

265   that crystallization had occurred. The particle morphology and Raman signals remained the same

266   when the RH was reduced further to 4.7 %, indicating no change in the crystal structure of the

267   $MgCl_2 \cdot 4H_2O$ particle. When this $MgCl_2 \cdot 4H_2O$ particle was subjected to a second humidification

268   process (Fig. 2c), the particles underwent a deliquescence transition at RH of 15.0–16.7 %. This

269   experiment suggests that the $MgCl_2 \cdot 6H_2O$ powder particles could not return to their original

270   form once they had been dissolved in the aqueous phase. For a nebulized, wet-deposited $MgCl_2$

271   aerosol particle, the RMS measurement results (Fig. 2d and e) indicated that it was crystalline

272   $MgCl_2 \cdot 4H_2O$, when dried after wet deposition. The crystalline particle dissolved at RH = 15.5–

273   16.5 % during the humidification process (Fig. 2d). And it crystallized back to $MgCl_2 \cdot 4H_2O$ at

274   RH = 7.2–6.8 % during the dehydration process (Fig. 2e), which are within the range of phase

275   transition RHs observed by OM.

276   The wet-deposited supermicron (1–10 μm) aqueous $MgCl_2$ droplets crystallized at a

277   lower solvated state ($MgCl_2 \cdot 4H_2O$) when RH was decreased to ~10.1–3.2 % (OM), rather than

278   the stable crystalline $MgCl_2 \cdot 6H_2O$. In the observed ERH range of ~10.1–3.2 %, the H_2O to Mg^{2+}

279   molar ratio, calculated from the AIOMFAC model (at high supersaturation), was in the range of

280   5.6–4.1. The calculated molar ratio is less than the 6 required for the hexahydrate, but > 4,

281   supporting the observed crystallization as the tetrahydrate. For bulk crystalline $MgCl_2 \cdot 6H_2O$,

282   Mg^{2+} ions are solvated first as $[Mg(6H_2O)]^{2+}$ in an octahedral structure and Cl^- ions are attached

283   to this hydrate (Casillas-Ituarte et al., 2010; Callahan et al., 2010; Hennings et al., 2013). During

284   the dehydration process of $MgCl_2$ droplets, the rate of the RH change in the measurement time-

285   scale of 2 min for recording each optical image and even 10 min for recording the Raman spectra

286   of an ensemble of particles appears to be insufficient for the thermodynamically predicted but

287   complex crystalline $MgCl_2 \cdot 6H_2O$ structure to take shape. This indicates the presence of a large

288   kinetic barrier and/or diffusional resistance to the hydrate-ion $[Mg(6H_2O)]^{2+}$ mobilization and

289   nucleation required for the structural growth and crystallization of $MgCl_2 \cdot 6H_2O$ with decreasing

290 availability of condensed water. However, it should be noted that under ambient conditions RH
291 changes can be more abrupt.

292   The thermodynamic properties for the dissolution of different hydrates in $MgCl_2 \cdot xH_2O$ (x
293 = 1, 2, 4, 6) at 298 K were reported to have large uncertainties (Wang et al., 1998), even though
294 anhydrous $MgCl_2$ was predicted to have the same DRH as crystalline $MgCl_2 \cdot 6H_2O$ at 298 K
295 (Kelly and Wexler, 2005). On the other hand, a higher free energy (less stable) and thus higher
296 solubility for $MgCl_2 \cdot 4H_2O$ than for $MgCl_2 \cdot 6H_2O$ can explain the current observation of a lower
297 DRH (15.9 ($\pm$0.3) %) for $MgCl_2 \cdot 4H_2O$ than for $MgCl_2 \cdot 6H_2O$ (~33 %).

298

299 **3.2 Hygroscopic behavior of NaCl–MgCl₂ mixture particles**

300   The theoretical aspects of the hygroscopic properties of binary mixture particles are
301 discussed in detail elsewhere (Li et al., 2014; Gupta et al., 2015). In general, for two-component
302 inorganic hygroscopic salt particles, the equilibrium thermodynamics predict two-stage
303 deliquescence and efflorescence transitions. During the humidification process, the first
304 deliquescence transition is due to dissolution of the eutonic component at a mutual DRH
305 (MDRH), which is independent of the mixing ratios; and the second transition due to the
306 complete dissolution of a residual solid component at a second DRH, which depends on the
307 mixing ratio of the two components (Wexler and Seinfeld, 1991). Similarly, during the
308 dehydration process, aqueous droplets with double salts should show stepwise efflorescence
309 transitions: a component of the aqueous droplets precipitates first at their specific ERH
310 depending on their mixing ratio and the remaining aqueous eutonic component effloresces at
311 their mutual ERH (MERH), which should be independent of the mixing ratios. Therefore,
312 effloresced particles can form a heterogeneous, core−shell crystal structure owing to the stepwise
313 crystallization process (Ge et al., 1996). Thermodynamic models, such as the Extended
314 Atmospheric Inorganics Model (E-AIM) (http://www.aim.env.uea.ac.uk/aim/aim.php) (Tang,
315 1976; Ansari and Pandis, 1999; Carslaw et al., 1995; Clegg et al., 1998a, b; Wexler and Clegg,
316 2002) and the AIOMFAC model (http://www.aiomfac.caltech.edu), can be used to predict the
317 MDRH and second DRHs. On the other hand, as efflorescence is a kinetic or rate-driven process
318 depending on many factors, no general theoretical model that covers the efflorescence of single
319 or multi-component aerosol particles is available (Seinfeld and Pandis, 2006; Cohen et al., 1987;

320 Martin, 2000). Moreover, it was observed that the physical state (i.e., amorphous or crystalline

321 and hydrated or anhydrous nature) of salts plays a vital role in water absorption, diffusion, uptake

322 or dissolution, evaporation, solidification, and morphology changes during the humidification

323 and dehydration processes (Mikhailov et al., 2009). Therefore, the best way to understand the

324 efflorescence behavior of aerosols is through experimental measurements (Seinfeld and Pandis,

325 2006).

326 Hygroscopic measurements were performed on 20-40 particles of each mixing ratio of

327 NaCl–MgCl$_2$ using OM. The hygroscopic behavior of the mixture particles could be divided into

328 three categories, (i) NaCl-rich of $X_{NaCl} \geq 0.3$, (ii) NaCl-rich of $X_{NaCl} = 0.05$, 0.1, and 0.2, and (iii)

329 MgCl$_2$-dominant particles of $X_{NaCl} = 0.01$ and 0.026 (the eutonic composition), which is

330 discussed in the following sections.

331 **3.2.1 NaCl-rich particles of $X_{NaCl} \geq 0.3$**

332 During the humidification process, NaCl–MgCl$_2$ particles with $X_{NaCl} \geq 0.3$ exhibit two

333 stage deliquescence transitions, as is generally expected for binary electrolytic mixture particles.

334 Figure 3 shows the 2-D area ratio plot for the humidification and dehydration processes as a

335 function of the RH for a NaCl-rich particle of $X_{NaCl} = 0.9$, which is similar to seawater ($X_{NaCl} = $

336 0.89) (Lide, 2002), together with the optical images shown at the transition points. Initially at RH

337 = 3.1 %, the optical image of the particle clearly shows its angular crystalline nature. During the

338 humidification process, the particle size remains constant until RH = ~14 %, where a slight

339 decrease in size is observed due to water adsorption at the lattice imperfections of the solid salts

340 in the particle and/or structural rearrangement inside the crystal lattice (Mikhailov et al., 2004;

341 Ahn et al., 2010). A first deliquescence transition was observed from RH = 15.1 to 15.8 %, where

342 the particle morphology changed somewhat at RH = 15.1 %, and the size increased noticeably at

343 RH = 15.8 %. With further increases in RH, the partially aqueous particle gradually grew until

344 RH = ~70.0 %, after which a sharp size increase was noted. The optical image at RH = 73.9 %

345 revealed a solid inclusion, which completely dissolved to form a homogeneous droplet, with the

346 second transition completing at RH = 74.1 %. Subsequently, with further increases in RH, the

347 aqueous droplet undergoes continuous hygroscopic growth, as shown for the larger droplet at RH

348 = 84.5 %. The first phase transition at RH = 15.8 %, i.e., MDRH of the NaCl–MgCl$_2$ system, is

12

349 assigned to the deliquescence of the $MgCl_2$-dominant eutonic solids in the particle. The observed

350 MDRH deviates from the calculated value of RH = 36.1 % according to the AIOMFAC model;

351 whereas it is comparable to the observed DRH (= 15.9 ($\pm$0.3) %) of crystalline $MgCl_2 \cdot 4H_2O$ for

352 nebulized pure $MgCl_2$. At the MDRH, the particle consists of a mixed phase of liquid droplets

353 (eutonic solution) and a NaCl solid inclusion, which is clearly visible in the optical image of the

354 droplet at RH = 73.9 %, just before the complete dissolution of pure NaCl at the second DRH of

355 74.1 %. The second DRH is consistent with the DRH of 74.1 % observed for a nascent SSA

356 particle levitated in an electro-dynamic balance (EDB) by Tang et al.(1997).

357   The other NaCl-rich particles with compositions of $X_{NaCl} \geq 0.3$ (e.g., X_{NaCl} = 0.5 in Fig.

358 4a) also exhibited two-stage phase transitions during the humidification process: the first

359 transition at MDRH (RH = 15.9 ($\pm$0.2) %) due to deliquescence of the eutonic component and

360 the second transition due to complete deliquescence of the particles. In the equimolar mixture

361 particles (X_{NaCl} = 0.5, Fig. 4a), the observed second DRH of 67.6 % (on average, 67.3 ($\pm$0.4) %,

362 in terms of reproducibility when the humidification and dehydration processes were repeated) is

363 consistent with the theoretical DRH of 67.5 % calculated using the AIOMFAC model. For an

364 equimolar mixing ratio, Chan et. al. (2000) estimated a MDRH of 32.0 % and a second DRH of

365 70 % from the phase diagram of the bulk $NaCl-MgCl_2-H_2O$ system. For the NaCl-rich particles

366 with compositions of $X_{NaCl} \geq 0.3$, the MDRH is independent of the compositions. On the other

367 hand, the second DRHs were dependent on the compositions and shift toward a pure NaCl limit

368 (DRH = 75.1 ($\pm$0.5) %) with increasing NaCl mole fraction, as observed for NaCl–KCl and

369 $NaCl-NaNO_3$ mixture particles (Li et al., 2014; Gupta et al., 2015).

370   During the dehydration process, the representative NaCl-rich particle of X_{NaCl} = 0.9 (Fig.

371 3) showed a two-stage phase transition. The liquid droplet decreased gradually in size with

372 decreasing RH and became supersaturated with respect to NaCl below RH of 74.1% (DRH for

373 X_{NaCl} = 0.9), where the droplet still appeared to be homogeneous (as shown in the optical image

374 at RH = 71.2 %). With the further decreases in RH, the droplet size decreased abruptly at RH =

375 45.9–45.6 % due to the crystallization of NaCl in the droplet. At RH = 45.6 %, the first ERH for

376 X_{NaCl} = 0.9, the particle was composed of a mixed phase of the eutonic solution and NaCl solids,

377 as observed clearly from the crystal segments in the optical image. With further decreases in RH,

378 the mixed phase droplet shrank gradually until RH = 5.3–5.1 %, where the $MgCl_2$-dominant

379   eutonic component in the particle crystallized. At RH = 5.1 % (MERH), a completely effloresced

380   solid particle was formed, which is clearly seen by the reappearance of an overall angular shape

381   and a bright crystalline segment in the optical image (similar to that at RH = 3.1 %, at the start of

382   the humidification process). The measured first ERH and MERH for the particles with a

383   composition of X_{NaCl} = 0.9 vary among the particles, 1−10 μm size, in the same optical image

384   field and are in the range, RH = 48.2–45.4 % and RH = 5.6–5.0 %, respectively.

385   During the dehydration process, the other NaCl-rich particles with compositions of X_{NaCl}

386   ≥ 0.3 also exhibited two-stage phase transitions. For example, for a particle with X_{NaCl} = 0.5 (Fig.

387   4a), the first transition due to the efflorescence of pure NaCl occurs at RH = 35.5–35.0 % and the

388   second due to the efflorescence of the eutonic component at RH = 5.7–5.5 %. Chan et al. (2000)

389   reported the first ERH of 38 % (within the range of the first ERHs of 40.5–35.0 % observed in

390   this study for 38 particles), but no MERH (in this work, it was observed in the RH range of 6.9–

391   5.0 %), when they performed the dehydration experiments on a single levitated aqueous droplet

392   of NaCl–MgCl$_2$ with an equimolar mixing ratio (X_{NaCl} = 0.5) in an EDB. The first ERHs for the

393   NaCl-rich mixture particles with compositions of X_{NaCl} ≥ 0.3 are dependent on the compositions

394   and shift toward the pure NaCl limit (ERH = 47.6–45.7 %) with increasing NaCl mole fraction,

395   as observed for NaCl-KCl and NaCl-NaNO$_3$ mixture particles (Li et al., 2014; Gupta et al.,

396   2015); whereas the MERH, like their MDRH, is almost independent of the particle compositions.

397   The MERHs, however, were observed over a wide RH range (RH = 10.4–2.9 %) due to the

398   stochastic nature of nucleation leading to efflorescence.

399   **3.2.2 NaCl-rich particles of X_{NaCl} = 0.05, 0.1, and 0.2**

400   In the case of NaCl-rich particles with compositions of X_{NaCl} = 0.1 and 0.2, three types of

401   particles showing 2- or 3-stage deliquescence transitions were observed. Figure 5a-c show the

402   hygroscopic behavior of representative "Types A, B, and C" particles, respectively, where their

403   particle/droplet optical images are also shown at each transition point. During the humidification

404   process, a Type A particle of X_{NaCl} = 0.2 (Fig. 5a) showed an initial small decrease in size due to

405   structural rearrangement before the first deliquescence transition at RH = 15.5–15.8 %. At its

406   MDRH of 15.8 %, bright solids in the particle disappeared due to dissolution of the eutonic

407   component. With further increases in RH, it gradually grew until RH = 56.7 %, after which an

14

408 abrupt increase in size was observed with the dissolution of pure NaCl, i.e., the second
409 deliquescence transition completing at RH of 57.0 % (resulting in a homogeneous droplet in the
410 optical image).

411   For Type B particles, three deliquescence transitions and one intermediate efflorescence
412 transition were observed during the humidification process (e.g., Fig. 5b). Figure 5b shows that
413 the particle size remained constant until RH = ~15.5 %, and then underwent an abrupt first
414 mutual deliquescence transition at RH of 15.5–15.8 % (called $MDRH_1$). The particle grew
415 gradually until the RH reached 21.9 %. Subsequently, an efflorescence-like transition with a
416 decrease in size and a bright, crystallized solid particle were observed at RHs of 21.9–24.9 %
417 and 24.9 %, respectively. Thereafter, the size of the Type B particle remained almost constant
418 until RH = 31.0 %, which was followed by a small decrease in size (structural rearrangement) at
419 RH = 32.0 % and then by a second mutual deliquescence transition at RH = 32.3–33.0 %
420 ($MDRH_2$). The observed $MDRH_2$ of 33.0 % for the Type B particle is attributed to the complete
421 dissolution of the crystalline $MgCl_2 \cdot 6H_2O$-dominant eutonic part. With further increases in RH,
422 the size of the Type B particle increased gradually until the third deliquescence transition with
423 the dissolution of pure NaCl (NaCl solid inclusion in the optical image at RH = 56.7 %
424 disappears in the optical image at RH = 57.0 %), which occurs at RH of 56.7–57.0 %, similar to
425 the Type A particle (Fig. 5a). The Type C particle (Fig. 5c) did not show the first deliquescence
426 transition at RH of ~ 15.8 % (seen in Fig. 5a and b) or recrystallization (seen in Fig. 5b), but its
427 size remained unchanged until RH = 31.0 %, followed by a small decrease in size due to the
428 structural rearrangement at RH = 32.0 %, and a sharp increase in size from RH = 32.3 − 33.0 %,
429 which is the first deliquescence transition or MDRH. The second deliquescence transition was
430 observed as usual at RH = 56.7 − 57.0 %.

431   During the dehydration process, the NaCl-rich particles of X_{NaCl} = 0.2 of Types A-C
432 particles showed two-stage phase transitions (Fig. 5a-c). The liquid droplets decreased gradually
433 in size with decreasing RH and became supersaturated with NaCl below RH = 57.0 % (DRH for
434 X_{NaCl} = 0.2). With further decreases in RH, the droplet sizes decreased noticeably at RH =
435 24.1–23.9 % for Type A particles (Fig. 5a), RH = 25.1–24.9 % for Type B particles (Fig. 5b), and
436 RH = 24.9–23.9 % for Type C particles (Fig. 5c), due to the crystallization of NaCl. At the first
437 ERHs of 23.9, 24.9, and 23.9 %, the partially aqueous Types A-C particles, respectively, are

15

438   composed of a mixed phase of a eutonic solution and NaCl solid. With further decreases in RH,

439   Types A and B droplets gradually shrank until the final perceptible decreases in sizes were

440   observed at RH = 6.1–5.2 % (Fig. 5a) and at RH = 5.4–5.2 % (Fig. 5b), where completely

441   effloresced Types A and B solid particles, respectively, were formed. Their low MERH of 5.2 %

442   suggests that the $MgCl_2 \cdot 4H_2O$-dominant eutonic component was crystallized for the Types A and

443   B particles. For the Type C particle, complete efflorescence occurred at RH = 23.9–23.7 % with

444   a MERH of 23.7 % (Fig. 5c). The high MERH suggests that the $MgCl_2$-dominant eutonic part

445   crystallized heterogeneously as the $MgCl_2 \cdot 6H_2O$ moiety on crystalline NaCl seeds, leading to the

446   observed MDRH of ~ 33.0 % for the Type C particle.

447   To clearly explain the above observations, particles with a composition of $X_{NaCl} = 0.2$

448   sitting on a Parafilm-M substrate were examined using in-situ RMS. Figure 6 shows the Raman

449   spectra and corresponding optical images, which were recorded during the in-situ RMS

450   measurements of particles of $X_{NaCl} = 0.2$. As shown in Fig. 6a, at RH = 4.5 %, the Type A particle

451   appears irregular and shows a typical –OH stretching signature for crystalline $MgCl_2 \cdot 4H_2O$. At

452   RH = 16.6 %, the Type A particle becomes round-shaped and the broad –OH stretching peak for

453   free-water indicates that it is deliquesced. During the dehydration process, as shown in Fig. 6b,

454   the Type A round droplet at RH = 10.7 % becomes irregular-shaped, i.e., effloresces at RH =

455   7.6 %, forming a crystalline $MgCl_2 \cdot 4H_2O$-dominant eutonic phase. For Type A particles, the

456   NaCl and $MgCl_2 \cdot 4H_2O$-dominant eutonic solids are dissolved and formed during the

457   humidification and dehydration processes.

458   As shown in Fig. 6c, during the humidification process, the Type B particle appears

459   irregular at low RH (= 4.6 %) and shows a –OH stretching signature for crystalline $MgCl_2 \cdot 4H_2O$.

460   At RH = 16.4 %, the particle becomes round and the broad –OH stretching signal for free water

461   indicates that it is deliquesced. With a small increase in RH (to ~16.6 %), however, the Type B

462   particle changes its morphology and shows the typical –OH vibration signatures for crystalline

463    $MgCl_2 \cdot 6H_2O$, indicating the occurrence of efflorescence. At RH = 33.9 %, the Type B particle

464   appears round and shows a free water –OH peak again, indicating that further deliquescence

465   occurs below RH = 33.9 %. During the dehydration process, as shown in Fig. 6d, the Type B

466   round droplet at RH = 15.3 % becomes irregular-shaped, i.e., effloresces at RH = 10.1 %,

467   forming a crystalline $MgCl_2 \cdot 4H_2O$-dominant eutonic phase. For Type B particles, NaCl and

16

468   MgCl$_2$·4H$_2$O-dominant eutonic solids are formed during the dehydration process, and despite the

469   MgCl$_2$·4H$_2$O-dominant eutonic solids being dissolved, the MgCl$_2$·6H$_2$O-dominant eutonic solids

470   are formed through efflorescence and are dissolved, and finally, the NaCl solids deliquesce

471   during the humidification process. Efflorescence of laboratory-generated particles during

472   humidification has not been reported previously.

473   As shown in Fig. 6f, at RH = 4.5 %, a Type C particle appears irregular and crystalline

474   and shows the typical –OH stretching signature for crystalline MgCl$_2$·6H$_2$O. At RH = 34.1 %, the

475   Type C particle appears round and shows a free water –OH peak, indicating that deliquescence

476   occurs below RH = 34.1 %. As shown in Fig. 6e, the Type C particle effloresced at a higher ERH

477   of 16.8 % and shows a typical –OH stretching signature for crystalline MgCl$_2$·6H$_2$O. For the

478   Type C particles, NaCl and MgCl$_2$·6H$_2$O-containing crystals are formed and dissolved during the

479   dehydration and humidification processes, as clearly confirmed by the OM and in-situ RMS

480   measurements. On the other hand, this Type C particle does not form MgCl$_2$·6H$_2$O again at the

481   next dehydration process, as shown in Fig. 6g, indicating that this particle is no longer Type C

482   and the different types of particles are formed somewhat randomly because efflorescence is a

483   kinetic or rate-driven process depending on many factors.

484   Table 1 shows the encountering frequencies of Types A-C particles at various NaCl-

485   MgCl$_2$ mixing ratios in their respective OM experiments. For all mixing ratios except X_{NaCl} = 0.1

486   and 0.2, Type A particles, which form a crystalline MgCl$_2$·4H$_2$O-dominant eutonic phase at

487   MERH, are dominant. Owing to the decreasing availability of condensed water during

488   dehydration, large kinetic barrier and/or diffusional resistance for hydrate-ion nucleation make

489   the formation of the crystalline MgCl$_2$·6H$_2$O structure difficult, which is already discussed for

490   the nebulized pure MgCl$_2$ aerosols.

491   For particles of X_{NaCl} = 0.1 and 0.2, the encountering frequencies of the Type B particles

492   are 29 % and 45 %, respectively, and Type C are 47 % and 18 %, respectively, indicating that the

493   formation of MgCl$_2$·6H$_2$O-containing crystals is easier at these mixing ratios. Aqueous moieties

494   in particles were reported to effloresce more easily by heterogeneous nucleation in the presence

495   of seeds (Schlenker and Martin, 2005; Li et al., 2014; Gupta et al., 2015). For Type C particles,

496   the crystallization of MgCl$_2$·6H$_2$O takes place at an ERH range of 23.7–11.9 % during

497   dehydration (e.g., see Fig. 5c), suggesting that the NaCl crystals of an optimal size (X_{NaCl} = 0.1

498   and 0.2) can act as seeds for the heterogeneous during the humidification process was once rep

499   nucleation of $MgCl_2 \cdot 6H_2O$. Heterogeneous nucleation of $(NH_4)_2SO_4$ in presence of optimally

500   sized kaolinite seeds was also reported by Pant et al (2006). On the other hand, the

501   heterogeneous efflorescence of $MgCl_2 \cdot 6H_2O$ is also observed during the humidification process

502   for Type B particles (Fig. 5b). Efflorescence orted for Amazonian rain-forest aerosols (Pöhlker et

503   al., 2014), where it was claimed that the impacted ambient organic–inorganic mixed aerosols

504   initially had amorphous or poly-crystalline structures and underwent restructuring through

505   kinetic water and ion mobilization, resulting in the crystallization of inorganic salts during

506   hydration. During the humidification process, the $MgCl_2 \cdot 4H_2O$-dominant eutonic solids in the

507   effloresced Type B particles of $X_{NaCl} = 0.1$ and 0.2 dissolve at $MDRH_1$ (= 15.9 (±0.3) %) and

508   some moisture is also adsorbed on the surface of the crystalline NaCl moiety. The $[Mg(6H_2O)]^{2+}$

509   hydrate-ions appear to be mobilized in the presence of sufficient condensed water at the observed

510   ERH range of ~ 16.1–24.9 % during hydration (~23.7–11.9 % during dehydration) and the

511   kinetic barrier is overcome by heterogeneous nucleation on the optimally-sized NaCl seeds,

512   leading to structural growth and crystallization of the $MgCl_2 \cdot 6H_2O$ moiety. Therefore, particles

513   of $X_{NaCl} = 0.1$ and 0.2 frequently show a characteristic MDRH of ~ 33.0 (±0.5) % for the

514   dissolution of the $MgCl_2 \cdot 6H_2O$-dominant eutonic solids. On the other hand, the crystalline NaCl

515   seeds for the particles of $X_{NaCl} \geq 0.3$, being larger than the optimal size, appear to inhibit the

516   smooth diffusion of water kinetically, which is a primary requirement for the nucleation of

517    $[Mg(6H_2O)]^{2+}$. Therefore, for particles of $X_{NaCl} \geq 0.3$, crystalline $MgCl_2 \cdot 6H_2O$ is not formed in

518   the timescale of the measurements.

519   In the case of particles of $X_{NaCl} = 0.05$, two-stage deliquescence transitions for Type A

520   particles were mainly observed: mutual deliquescence occurring at MDRH of 16.0 (±0.3) % and

521   the second DRH for the remnant NaCl at RH of 40.5 (±1.5) %. For $X_{NaCl} = 0.05$, the frequency

522   with which particles of Types B and C were encountered was much lower (Table 1), most likely

523   because the NaCl seeds were smaller than the optimal size.

524   For the NaCl-rich particles of $X_{NaCl} = 0.05$, 0.1, and 0.2, the second DRHs were

525   dependent on the compositions and shifted toward the pure NaCl limit (DRH= 75.1 (±0.5) %)

526   with increasing NaCl mole fraction. Figure 7 plots the measured DRHs for the NaCl-rich

527   particles with various compositions as a function of the NaCl mole fraction, showing that the

528 experimental second DRH values are in good agreement with the values calculated from the
529 AIOMFAC model. On the other hand, the observed MDRH (= 15.9 ($\pm$0.3) %) for Type A
530 particles deviates from that predicted by the thermodynamic considerations in the model. In
531 contrast, the observed $MDRH_2$ for the Type B particles and MDRH for the Type C particle of
532 33.0 ($\pm$0.5) % agree with the predicted DRH for $MgCl_2 \cdot 6H_2O$.

533   In the case of $X_{NaCl} = 0.2$, the measured first ERH and MERH vary among Types A and B
534 particles, 1$-$10 μm in size, on the same optical image field and are in the range of RH = 27.1$-$
535 23.9 % (average first ERH = 25.0 %) and RH = 10.2$-$5.2 % (average MERH = 7.1 %),
536 respectively. In contrast, the Type C particles exhibit MERH in the range of 23.7$-$15.3 %
537 (average MERH = 18.1 %). For Types A and B particles of $X_{NaCl} = 0.1$, the measured first ERH
538 and MERH vary in the range of RH = 17.4$-$12.4 % (average first ERH = 15.8 %) and RH = 9.4$-$
539 6.5 % (average MERH = 7.2 %), respectively, whereas the Type C particles exhibit MERH in the
540 range of 15.2$-$11.9 % (average MERH = 13.3 %). In the case of $X_{NaCl} = 0.05$, the measured first
541 ERH and MERH vary in the range of RH = 15.5$-$13.0 % (average first ERH = 13.2 %) and RH =
542 9.3$-$6.5 % (average MERH = 6.9 %), respectively. Figure 8 shows the measured ERHs for the
543 NaCl-rich particles with various compositions as a function of the NaCl mole fraction.

544 **3.2.3 $MgCl_2$-dominant particles of $X_{NaCl} = 0.01$ and 0.026 (the eutonic composition)**

545   Figure 4b and c present the 2-D area ratio plots for the $MgCl_2$-dominant particles with the
546 eutonic composition ($X_{NaCl} = 0.026$) and of $X_{NaCl} = 0.01$ as a function of RH. During the
547 humidification process, the particles of $X_{NaCl} = 0.026$ and 0.01 show single-stage deliquescence
548 phase transitions from RH = 15.7 to 16.1 % and from RH = 15.6 to 16.1 %, respectively. With
549 further increases in RH, the particles showed continuous and gradual hygroscopic growth.
550 During the dehydration process, the particles of $X_{NaCl} = 0.026$ and 0.01 decreased gradually in
551 size until they exhibited hysteresis with single-stage efflorescence transitions from RH = 5.3 to
552 4.5 % and from RH = 4.8 to 4.6 %, respectively. Therefore, the hygroscopic behavior of these
553 particles with $MgCl_2$-dominant compositions is similar to that of the nebulized pure $MgCl_2$
554 particles (Fig. 1b).

555   The probability of forming a crystalline $MgCl_2 \cdot 6H_2O$ structure for particles of $X_{NaCl} =$
556 0.026 and 0.01 is quite low (Table 1), due to the low probability of heterogeneous nucleation in

19

557   the absence of optimally-sized seeds, as explained above for the case of $X_{NaCl} = 0.05$. NaCl,

558   which is mostly in the aqueous phase, cannot act as a crystalline seeds for heterogeneous

559   nucleation at low RHs, or the sizes of those NaCl seeds are too small for heterogeneous

560   nucleation leading to the formation of a hexahydrate ($MgCl_2 \cdot 6H_2O$) structure.

3.3 Deliquescence phase diagram of mixed NaCl-MgCl₂ particles

562   Figure 7 presents the measured first or second MDRHs ($MDRH_1$ or $MDRH_2$) and second

563   DRHs of the NaCl−MgCl₂ mixture particles with different mole fractions along with the

564   measured DRHs of the pure NaCl and MgCl₂ particles. As shown in Fig. 7, a clearly demarked

565   phase diagram depicting their deliquescence behavior was obtained experimentally for the first

566   time, for which, until now, there was no experimental data to the best of the authors' knowledge;

567   1. NaCl(s) + MgCl₂(s) phase: both NaCl and MgCl₂ are mixed as solids below the MDRHs

568   at all mole fractions;

569   2. NaCl(s) + eutonic(aq) phase: a mixed phase of solid NaCl and aqueous eutonic

570   components between the MDRHs and second DRHs for $X_{NaCl} > 0.026$;

571   3. NaCl(aq) + MgCl₂(aq) phase: both NaCl and MgCl₂ are mixed in the aqueous phase

572   above the second DRHs at all mole fractions.

573   The second DRHs obtained experimentally agree well with the values calculated from the

574   ionic activity products of the constituents predicted by the AIOMFAC model, as shown in Fig. 7

575   (dash-dotted curve for the second DRHs). On the other hand, the observed $MDRH_1$ (= 15.9

576   (± 0.3) %) for most particles (of all mole fractions) was lower than the MDRH values of 36.1 %

577   calculated from the AIOMFAC model and 32.0 % estimated using the bulk NaCl−MgCl₂−H₂O

578   system phase diagram (Tang, 1976; Chan et al., 2000). This is similar to the case observed for the

579   nebulized pure MgCl₂. On the other hand, particles with compositions of $X_{NaCl} = 0.1$ and 0.2

580   frequently show two MDRHs at 15.9 (± 0.3) % ($MDRH_1$) and 33.0 (± 0.5) % ($MDRH_2$). The

581   dense ($0.1 \leq X_{NaCl} \leq 0.2$) and light ($0.01 \leq X_{NaCl} \leq 0.05$) brown shaded patterns in Fig. 7 indicate

582   the high and low frequencies for encountering $MDRH_2$, respectively (Table 1). The eutonic

583   composition ($X_{NaCl} = 0.026$), which was calculated theoretically from the AIOMFAC model,

584   cannot be ascertained clearly from the experimental data as the deliquescence transition for these

585   MgCl$_2$-dominant compositions (Fig. 4b and c) becomes similar to that of the nebulized pure

586   MgCl$_2$ (Fig. 1b). On the other hand, it should be close to the value of X_{NaCl} = 0.029 (NaCl = ~

587   1% and MgCl$_2$ = ~ 35 %) calculated from the phase diagram for the bulk NaCl–MgCl$_2$–H$_2$O

588   system at 298.15 K based on equilibrium thermodynamics (Seidell and Linke, 1965; Tang, 1976).

589   Chan et al. (2000) calculated a MDRH of 32.0 % and a second DRH of 70 % for an equimolar

590   mixing ratio from the bulk NaCl–MgCl$_2$–H$_2$O system phase diagram (Seidell and Linke, 1965),

591   but no experimental DRHs were reported.

592   All the mixed NaCl–MgCl$_2$ particles showed the first deliquescence transition at the

593   MDRH$_1$ (= 15.9 (±0.3) %), regardless of the mixing ratio of the two salts, except for

594   compositions of $0.01 \leq X_{NaCl} \leq 0.2$, particularly X_{NaCl} = 0.1 and 0.2, where Types B and C

595   particles also exhibited a partial deliquescence transition at MDRH$_2$ (= 33.0 (±0.5) %) for the

596   crystalline MgCl$_2$·6H$_2$O-dominant eutonic components. Thermodynamically, as the first

597   deliquescence transition of mixed-salts is governed by the water activity at the eutonic point, the

598   MDRH of the mixed-salt particles is normally independent of the initial composition of the

599   mixture. For the NaCl-rich particles of X_{NaCl} > 0.026, which contain more NaCl than the eutonic

600   composition, as the NaCl mole fraction increases, the second DRH values approach the DRH of

601   the pure NaCl salt. This suggests that for particles with X_{NaCl} > 0.026, the second-stage

602   deliquescence is driven purely by the solid NaCl remaining after deliquescence of the eutonic

603   composition (Li et al., 2014; Gupta et al., 2015).

604   **3.4 Efflorescence phase diagram of mixed NaCl-MgCl$_2$ particles**

605   Figure 8 shows the measured ERHs and MERHs for mixed NaCl–MgCl$_2$ particles with

606   various mixing ratios as a function of the NaCl mole fraction. Similar to the deliquescence phase

607   diagram, which showed three systematic phases, the efflorescence phase diagram is also

608   composed of three distinct phases:

609   1. NaCl(aq) + MgCl$_2$(aq) phase: both NaCl and MgCl$_2$ are mixed in the aqueous phase

610   above the first ERHs at all mixing ratios;

611   2. NaCl(s) + eutonic(aq) phase: a mixed phase of solid NaCl and aqueous eutonic

612   components between the first ERH and second ERH (MERH) for X_{NaCl} > 0.026; and

613   3.   NaCl(s) + MgCl$_2$(s) phase: both NaCl and MgCl$_2$ are mixed as solids below the second

614   ERH (MERH) for $X_{NaCl} > 0.026$ and below the first ERHs for $X_{NaCl} \leq 0.026$.

615   To the best of the authors' knowledge, this is the first experimental phase diagram for

616   efflorescence of mixed NaCl–MgCl$_2$ particles. The first ERHs of NaCl-rich droplets ($X_{NaCl} >$

617   0.026) shift toward the pure NaCl limit (RH = 47.6 − 45.7 %) with increasing NaCl mole fraction

618   (see Fig. 8). This suggests that the first-stage efflorescence for particles of $X_{NaCl} > 0.026$ is driven

619   purely by the homogeneous nucleation of NaCl, the rate of which increases with increasing NaCl

620   mole fraction (Gupta et al., 2015). Chan et al. (2000) reported that the first ERH for the

621   crystallization of pure NaCl is 38.0 % for an equimolar mixing ratio, which is within the range of

622   the first ERH of 40.3 − 35.0 % (Figs. 4a and 8) measured for the same mixing ratio in the present

623   work. Although they did not report MERH, MERHs were clearly observed in this study. For

624   Types A and B particles, the measured MERH$_1$ were observed over a wide range (~ 10.4–2.9 %)

625   because of the stochastic nucleation events leading to the crystallization of MgCl$_2 \cdot$4H$_2$O moieties.

626   The MERH$_1$ range is similar to that for the nebulized pure MgCl$_2$ particles (ERH = 10.1–3.2 %).

627   On the other hand, MERH$_2$ values for Type C particles of $X_{NaCl} = 0.1$ and 0.2 were in the ranges

628   of ~15.2–11.9 % and ~23.7–15.3 %, which is just below their first ERHs of ~17.4–12.4 % and

629   ~27.1–23.9 %, respectively, because the optimally-sized NaCl seeds, which are needed to

630   facilitate heterogeneous nucleation leading to the crystallization of MgCl$_2 \cdot$6H$_2$O, are available

631   immediately after the first efflorescence transitions. The droplets with MgCl$_2$-dominant

632   compositions, such as $X_{NaCl} = 0.026$ and 0.01, showed the single efflorescence transitions over an

633   ERH range of 9.7–3.4 % and 6.2–4.0 %, respectively.

634

635   **3.5 Spatial distribution of effloresced NaCl- MgCl$_2$ solid particles**

636   SEM/EDX was used to examine the morphology and spatial distribution of the chemical

637   components in the effloresced NaCl–MgCl$_2$ solid particles at various mixing ratios after the

638   humidification and dehydration cycles. Figure 9A and B shows elemental X-ray mapping images

639   for Na, Mg, O, and Na/Mg (mixed) and a secondary electron image (SEI) of NaCl-rich particles

640   with $X_{NaCl} = 0.9$ (seawater-like mixing ratio) and $X_{NaCl} = 0.6$, respectively. The elemental X-ray

641   maps in both cases suggest that Na (from NaCl) is concentrated in the central part, whereas Mg

642 and O (from $MgCl_2 \cdot 4H_2O$) are more concentrated at the edges. This suggests that NaCl nucleates

643 homogeneously to crystallize in the center at the first ERH, whereas the $MgCl_2 \cdot 4H_2O$-dominant

644 eutonic phase solidifies on these central NaCl seeds at the second ERH (MERH), corroborating

645 the efflorescence mechanism observed by OM. $MgCl_2$-rich or $MgCl_2$-dominant particles were

646 not shown because $MgCl_2$ covers whole particles without a visible NaCl moiety and their

647 hygroscopic behavior is similar to that of the nebulized pure $MgCl_2$ particles.

648 **3.6 Atmospheric implications**

649   Because Cl^- is the most abundant anion, and Na^+ and Mg^{2+} are the first and second most

650 abundant cationic species, respectively, in nascent sea-salt (Seinfeld and Pandis, 2006),

651 NaCl–$MgCl_2$ binary mixture particles can be good surrogates for the nascently generated

652 inorganic-rich supermicron SSAs. For particles with an approximately seawater-like mixing ratio

653 of $X_{NaCl} = 0.9$, the hygroscopic curve (2-D area ratio plots as a function of RH, as shown in Fig.

654 3) is similar to those obtained by OM for the particles nebulized from artificial seawater

655 (Schindelholz et al., 2014) and by EDB measurements on sea-salt particles generated from

656 filtered seawater (Tang et al., 1997). In addition, the hygroscopic curve for particles of $X_{NaCl} =$

657 0.9 is similar to that obtained for genuine ambient SSAs (Ahn et al., 2010), except that the real

658 genuine SSAs, having other minor chemical species, such as Ca^{2+}, K^+, SO_4^{2-}, and organics, did

659 not show distinct MDRH or MERH, as observed in this study for the case of $X_{NaCl} = 0.9$. On the

660 other hand, the hygroscopic behavior and growth curve in Fig.e 3 deviated considerably from

661 that of pure NaCl particles, as shown in Fig. 1a and by previous reports (Tang et al., 1997; Ahn et

662 al., 2010; Schindelholz et al., 2014). These observations suggest that pure $MgCl_2$ species (Fig.

663 1b) plays a strong role in the hygroscopicity of the NaCl–$MgCl_2$ mixture system as well as the

664 nascent ambient SSAs.

665   Mg^{2+}, residing at the edges (core-shell type micro-structure, as shown in Fig. 9) and

666 being in an aqueous phase even at very low RHs, i.e., at RHs higher than ~15.9 % and ~5 % in

667 the humidification (Fig. 7) and dehydration (Fig. 8) modes, respectively, may have important

668 implications for nascent SSA heterogeneous chemistry (Wise et al., 2009; Woods et al., 2010;

669 Woods et al., 2012; Liu et al., 2007; Ault et al., 2013). As NaCl–$MgCl_2$ binary mixture particles

670 can maintain an aqueous phase over a much broader RH range than pure NaCl particles, they

671 will be increasingly susceptible to reactions with gas phase inorganic and organic species, such

672 as NO_x, SO_x, HNO_3/H_2SO_4, and dicarboxylic acids (DCAs). Liu et al. (2007) reported the faster

673 uptake of gaseous HNO_3 into $NaCl–MgCl_2$ mixture particles with a seawater-like mixing ratio

674 and ambient SSAs than into pure NaCl particles. The lack of knowledge, however, of the

675 hygroscopic behavior and phases of $NaCl–MgCl_2$ mixture particles has resulted in large

676 uncertainties for the determination of the uptake coefficient of HNO_3. Therefore, in terms of the

677 aqueous phase chemistry of nascent SSAs, the hygroscopic behavior of $NaCl–MgCl_2$ mixture

678 particles, systematically investigated in this study for the first time, is of higher relevance as

679 nascent SSA surrogates than pure NaCl particles.

680   The NaCl moiety, crystallizing easily at higher RHs than $MgCl_2$, and the aqueous Mg^{2+}

681 moiety, having a high surface tension and viscosity, may have a tendency to separate or

682 fractionate in ambient SSAs. These chemical fractionations can occur even during wave breaking

683 or bubble bursting processes on the sea surface (Keene et al., 2007) and due to high wind speeds

684 (Gaston et al., 2011). Therefore, fractionated NaCl-rich and $MgCl_2$-rich particles have often been

685 reported for ambient SSAs (Wise et al., 2007; Ahn et al., 2010; Gaston et al., 2011; Hara et al.,

686 2014; Prather et al., 2013). Both ambient and laboratory-generated SSAs show that organic

687 species are mostly associated with Mg-rich inorganics (Keene et al., 2007; Prather et al., 2013).

688 The unexpectedly low MDRH and MERH of $MgCl_2 \cdot 4H_2O$ moiety and the stochastic nature of

689 heterogeneous nucleation for $MgCl_2 \cdot 6H_2O$ formation in the presence of optimally-sized seeds,

690 together with the presence of organics, may partially explain the intriguing hygroscopic behavior

691 of SSAs (Meskhidze et al., 2013). The heterogeneous crystallization of $MgCl_2 \cdot 6H_2O$ can also

692 take place in the presence of other seeds in SSAs, such as easily crystallizing $CaSO_4$ (ERH =

693 80–90 %) (Xiao et al., 2008). Therefore, the hygroscopic properties of all mixing ratios of the

694 $NaCl–MgCl_2$ system covered in this study, including the $MgCl_2$-rich/dominant particles, can

695 provide some insight into the physico-chemical characteristics and atmospheric chemistry of

696 nascent SSAs.

697

698 **4. CONCLUSIONS**

699   The hygroscopic properties, physical states/phases and chemical micro-structures of pure

700 $MgCl_2$ particles and the two-component $NaCl–MgCl_2$ mixture particles deposited on substrates

were studied by OM, in-situ RMS, and SEM/EDX elemental X-ray mapping. The DRHs and ERHs of laboratory-generated aerosol particles of 1-10 μm size at room temperature were determined by monitoring the 2-D area change for particles on optical images with RH variations between ~3 and 90 %. During the humidification process, wet-deposited particles from an $MgCl_2 \cdot 6H_2O$ solution showed a MDRH of 15.9 (± 0.3) %. The characteristic –OH vibration signatures from in-situ RMS indicated the formation of $MgCl_2 \cdot 4H_2O$, rather than thermodynamically stable $MgCl_2 \cdot 6H_2O$, due to a kinetic barrier to nucleation and structural growth with limited condensed water during the dehydration process. The NaCl–$MgCl_2$ mixture particles with NaCl-rich compositions of $0.05 \leq X_{NaCl} \leq 0.9$ mostly showed two-stage deliquescence: first, with the dissolution of eutonic components, and second, with the complete dissolution of NaCl, typical for two component salt systems (Gupta et al., 2015; Li et al., 2014). The second DRH values approach the pure NaCl limit as the mole fraction of NaCl increases. Interestingly, NaCl-rich particles with composition of $X_{NaCl} = 0.1$ and 0.2 showed three different mutual deliquescence behaviors during the humidification process, which was also confirmed by complementary in-situ RMS measurements. The first type showed an MDRH of 15.9 (±0.3) %; the second type showed a first MDRH at ~ 15.9 (±0.3) %, an efflorescence-like transition to $MgCl_2 \cdot 6H_2O$ at RH in the range of ~ 16.1–24.9 %, and a second MDRH at ~ 33.0 (±0.5) %; and the third type showed an MDRH at ~ 33.0 (±0.5) %. These phenomena are rarely observed for NaCl-rich particles of $0.3 \leq X_{NaCl} \leq 0.9$ and also $X_{NaCl} = 0.05$, where most particles showed an MDRH at ~ 15.9 (±0.3) %. Particles with $MgCl_2$-dominant compositions of $X_{NaCl} = 0.026$ (eutonic) and 0.01 mostly showed single-stage deliquescence behavior like pure $MgCl_2 \cdot 4H_2O$ particles with a DRH of 15.9 (±0.3) %.

During dehydration, NaCl–$MgCl_2$ mixture particles of $0.05 \leq X_{NaCl} \leq 0.9$ showed two-stage efflorescence: first, by the homogeneous nucleation of NaCl and second, by nucleation of the eutonic component at MERH, which is mostly independent of the aerosol compositions. The first ERH values approach the pure NaCl limit as the mole fraction of NaCl increases. $MgCl_2$-dominant particles with the eutonic composition ($X_{NaCl} = 0.026$) and $X_{NaCl} = 0.01$ showed single-stage efflorescence at ERHs ranging from 10.1 to 3.2 %. Most particles at all mixing ratios ($0.01 \leq X_{NaCl} \leq 0.9$) showed MERHs in the range of 10.4–2.9 %, forming $MgCl_2 \cdot 4H_2O$. On the other hand, a significant number of particles with $X_{NaCl} = 0.1$ and 0.2 were observed to undergo a

second efflorescence at higher MERHs = 15.2–11.9 % and 23.7–15.3 %, respectively, to form $MgCl_2 \cdot 6H_2O$, which is coupled with the observation of the first MDRH at ~ 33.0 % during the subsequent humidification process. The observation of $MgCl_2 \cdot 6H_2O$ efflorescence at relatively higher RH ranges than $MgCl_2 \cdot 4H_2O$ efflorescence suggests that the presence of sufficient condensed water assists in hydrate-ion $[Mg(6H_2O)]^{2+}$ mobilization and that only optimally-sized crystalline NaCl can act as heterogeneous nucleation seeds to overcome the kinetic barrier, leading to the structural growth and crystallization of $MgCl_2 \cdot 6H_2O$. SEM/EDX elemental X-ray mapping showed that the effloresced $NaCl–MgCl_2$ particles of NaCl-rich mixing ratios had the NaCl moiety homogeneously crystallized in the center, surrounded by $MgCl_2 \cdot 4H_2O$, forming a core-shell structure.

NaCl–MgCl$_2$ mixture aerosol particles can maintain an aqueous phase over a wider RH range than the pure NaCl particles, both in the humidification and the dehydration modes, making their heterogeneous chemistry with atmospheric gas phase species more likely. The hygroscopic curves, Raman -OH vibrational signatures, phase diagrams obtained for DRHs and ERHs, and chemical X-ray maps of effloresced particles covering twelve mixing ratios ($0.01 \leq X_{NaCl} \leq 0.9$) provided a clear picture of the hygroscopic behavior and chemical micro-structure of NaCl–MgCl$_2$ mixture particles as nascent SSA surrogates. This can help characterize the mixing states, morphology, phases, and aqueous phase chemistry of ambient, nascent inorganic SSAs.

References

Ahn, K.-H., Kim, S.-M., Jung, H.-J., Lee, M.-J., Eom, H.-J., Maskey, S., and Ro, C.-U.: Combined Use of Optical and Electron Microscopic Techniques for the Measurement of Hygroscopic Property, Chemical

Composition, and Morphology of Individual Aerosol Particles, Anal. Chem., 82, 7999-8009, 10.1021/ac101432y, 2010.

Ansari, A. S., and Pandis, S. N.: Prediction of multicomponent inorganic atmospheric aerosol behavior, Atmos. Environ., 33, 745-757, doi: 10.1016/S1352-2310(98)00221-0, 1999..

Ault, A. P., Guasco, T. L., Ryder, O. S., Baltrusaitis, J., Cuadra-Rodriguez, L. A., Collins, D. B., Ruppel, M. J., Bertram, T. H., Prather, K. A., and Grassian, V. H.: Inside versus Outside: Ion Redistribution in Nitric Acid Reacted Sea Spray Aerosol Particles as Determined by Single Particle Analysis, J. Am. Chem. Soc., 135, 14528-14531, doi: 10.1021/ja407117x, 2013.

Callahan, K. M., Casillas-Ituarte, N. N., Roeselová, M., Allen, H. C., and Tobias, D. J.: Solvation of Magnesium Dication: Molecular Dynamics Simulation and Vibrational Spectroscopic Study of Magnesium Chloride in Aqueous Solutions, J. Phys. Chem. A, 114, 5141-5148, 10.1021/jp909132a, 2010.

Carslaw, K. S., Clegg, S. L., and Brimblecombe, P.: A Thermodynamic Model of the System HCl-HNO3-H2SO4-H2O, Including Solubilities of HBr, from < 200 to 328 K, J. Phys. Chem., 99, 11557-11574, doi: 10.1021/j100029a039, 1995.

Casillas-Ituarte, N. N., Callahan, K. M., Tang, C. Y., Chen, X., Roeselová, M., Tobias, D. J., and Allen, H. C.: Surface organization of aqueous MgCl2 and application to atmospheric marine aerosol chemistry, Proc. Natl. Acad. Sci., 107, 6616-6621, 10.1073/pnas.0912322107, 2010.

Chan, C. K., Ha, Z., and Choi, M. Y.: Study of water activities of aerosols of mixtures of sodium and magnesium salts, Atmos. Environ., 34, 4795-4803, http://dx.doi.org/10.1016/S1352-2310(00)00252-1, 2000.

Clegg, S. L., Brimblecombe, P., and Wexler, A. S.: Thermodynamic Model of the System H+−NH4+−SO42-−NO3-−H2O at Tropospheric Temperatures, J. Phys. Chem. A, 102, 2137-2154, 10.1021/jp973042r, 1998a.

Clegg, S. L., Brimblecombe, P., and Wexler, A. S.: Thermodynamic Model of the System H+−NH4+−Na+−SO42-−NO3-−Cl-−H2O at 298.15 K, J. Phys. Chem. A, 102, 2155-2171, 10.1021/jp973043j, 1998b.

Cohen, M. D., Flagan, R. C., and Seinfeld, J. H.: Studies of concentrated electrolyte solutions using the electrodynamic balance. 3. Solute nucleation, J. Phys. Chem., 91, 4583-4590, 10.1021/j100301a031, 1987.

Cziczo, D. J., Nowak, J. B., Hu, J. H., and Abbatt, J. P. D.: Infrared spectroscopy of model tropospheric aerosols as a function of relative humidity: Observation of deliquescence and crystallization, J. Geophys. Res. — Atmos., 102, 18843-18850, 10.1029/97jd01361, 1997.

Cziczo, D. J., and Abbatt, J. P. D.: Infrared Observations of the Response of NaCl, MgCl2, NH4HSO4, and NH4NO3 Aerosols to Changes in Relative Humidity from 298 to 238 K, J. Phys. Chem. A, 104, 2038-2047, 10.1021/jp9931408, 2000.

Drozd, G., Woo, J., Häkkinen, S. A. K., Nenes, A., and McNeill, V. F.: Inorganic salts interact with oxalic acid in submicron particles to form material with low hygroscopicity and volatility, Atmos. Chem. Phys., 14, 5205-5215, 10.5194/acp-14-5205-2014, 2014.

Eom, H.-J., Gupta, D., Li, X., Jung, H.-J., Kim, H., and Ro, C.-U.: Influence of Collecting Substrates on the Characterization of Hygroscopic Properties of Inorganic Aerosol Particles, Anal. Chem., 86, 2648-2656, 10.1021/ac4042075, 2014.

Finlayson-Pitts, B. J., and Pitts, J. N.: Chemistry of the upper and lower atmosphere : theory, experiments, and applications, Academic Press, San Diego, xxii, 969 p. pp., 2000.

Gaston, C. J., Furutani, H., Guazzotti, S. A., Coffee, K. R., Bates, T. S., Quinn, P. K., Aluwihare, L. I., Mitchell, B. G., and Prather, K. A.: Unique ocean-derived particles serve as a proxy for changes in ocean chemistry, J. Geophys. Res. — Atmos., 116, D18310, doi: 10.1029/2010jd015289, 2011.

Ge, Z., Wexler, A. S., and Johnston, M. V.: Multicomponent Aerosol Crystallization, J. Colloid Interface Sci., 183, 68-77, http://dx.doi.org/10.1006/jcis.1996.0519, 1996.

Ghorai, S., Wang, B., Tivanski, A., and Laskin, A.: Hygroscopic Properties of Internally Mixed Particles Composed of NaCl and Water-Soluble Organic Acids, Environ. Sci. Technol., 48, 2234-2241, 10.1021/es404727u, 2014.

Gough, R. V., Chevrier, V. F., and Tolbert, M. A.: Formation of aqueous solutions on Mars via deliquescence of chloride–perchlorate binary mixtures, Earth and Planetary Science Letters, 393, 73-82, http://dx.doi.org/10.1016/j.epsl.2014.02.002, 2014.

Gupta, D., Kim, H., Park, G., Li, X., Eom, H. J., and Ro, C. U.: Hygroscopic properties of NaCl and NaNO3 mixture particles as reacted inorganic sea-salt aerosol surrogates, Atmos. Chem. Phys., 15, 3379-3393, 10.5194/acp-15-3379-2015, 2015.

Ha, Z., and Chan, C. K.: The Water Activities of MgCl2, Mg(NO3)2, MgSO4, and Their Mixtures, Aerosol Sci. Technol., 31, 154-169, 10.1080/027868299304219, 1999.

Hara, K., Osada, K., Yabuki, M., and Yamanouchi, T.: Seasonal variation of fractionated sea-salt particles on the Antarctic coast, Geophys. Res. Lett., 39, L18801, doi: 10.1029/2012gl052761, 2012.

Hara, K., Nakazawa, F., Fujita, S., Fukui, K., Enomoto, H., and Sugiyama, S.: Horizontal distributions of aerosol constituents and their mixing states in Antarctica during the JASE traverse, Atmos. Chem. Phys., 14, 10211-10230, 10.5194/acp-14-10211-2014, 2014.

Haywood, J., and Boucher, O.: Estimates of the direct and indirect radiative forcing due to tropospheric aerosols: A review, Rev. Geophys., 38, 513-543, 10.1029/1999rg000078, 2000.

Hennings, E., Schmidt, H., and Voigt, W.: Crystal structures of hydrates of simple inorganic salts. I. Water-rich magnesium halide hydrates MgCl2·8H2O, MgCl2·12H2O, MgBr2·6H2O, MgBr2·9H2O, MgI2·8H2O and MgI2·9H2O, Acta Crystallographica Section C, 69, 1292-1300, 10.1107/s0108270113028138, 2013.

Keene, W. C., Maring, H., Maben, J. R., Kieber, D. J., Pszenny, A. A. P., Dahl, E. E., Izaguirre, M. A., Davis, A. J., Long, M. S., Zhou, X., Smoydzin, L., and Sander, R.: Chemical and physical characteristics of nascent aerosols produced by bursting bubbles at a model air-sea interface, J. Geophys. Res. — Atmos., 112, D21202, 10.1029/2007jd008464, 2007.

28

856 Kelly, J. T., and Wexler, A. S.: Thermodynamics of carbonates and hydrates related to heterogeneous
857 reactions involving mineral aerosol, J. Geophys. Res. — Atmos., 110, D11201, 10.1029/2004jd005583,
858 2005.
859
860 King, S. M., Butcher, A. C., Rosenoern, T., Coz, E., Lieke, K. I., de Leeuw, G., Nilsson, E. D., and Bilde,
861 M.: Investigating Primary Marine Aerosol Properties: CCN Activity of Sea Salt and Mixed Inorganic–
862 Organic Particles, Environ. Sci. Technol., 46, 10405-10412, 10.1021/es300574u, 2012.
863
864 Krieger, U. K., Marcolli, C., and Reid, J. P.: Exploring the complexity of aerosol particle properties and
865 processes using single particle techniques, Chem. Soc. Rev., 41, 6631-6662, 10.1039/c2cs35082c, 2012.
866
867 Krueger, B. J., Grassian, V. H., Iedema, M. J., Cowin, J. P., and Laskin, A.: Probing Heterogeneous
868 Chemistry of Individual Atmospheric Particles Using Scanning Electron Microscopy and Energy-
869 Dispersive X-ray Analysis, Anal. Chem., 75, 5170-5179, 10.1021/ac034455t, 2003.
870
871 Li, X., Gupta, D., Eom, H.-J., Kim, H., and Ro, C.-U.: Deliquescence and efflorescence behavior of
872 individual NaCl and KCl mixture aerosol particles, Atmos. Environ., 82, 36-43,
873 http://dx.doi.org/10.1016/j.atmosenv.2013.10.011, 2014.
874
875 Lide, D. R.: Handbook of Chemistry and Physics Eighty third ed., edited by: Lide, D. R., CRC Press,
876 Boca Raton, Florida, 2002.
877
878 Liu, Y., Cain, J. P., Wang, H., and Laskin, A.: Kinetic Study of Heterogeneous Reaction of Deliquesced
879 NaCl Particles with Gaseous HNO3 Using Particle-on-Substrate Stagnation Flow Reactor Approach, J.
880 Phys. Chem. A, 111, 10026-10043, 10.1021/jp072005p, 2007.
881
882 Ma, Q., Ma, J., Liu, C., Lai, C., and He, H.: Laboratory Study on the Hygroscopic Behavior of External
883 and Internal C2–C4 Dicarboxylic Acid–NaCl Mixtures, Environ. Sci. Technol., 47, 10381-10388,
884 10.1021/es4023267, 2013.
885
886 Martin, S. T.: Phase Transitions of Aqueous Atmospheric Particles, Chem. Rev., 100, 3403-3454,
887 10.1021/cr990034t, 2000.
888
889 Meskhidze, N., Petters, M. D., Tsigaridis, K., Bates, T., O'Dowd, C., Reid, J., Lewis, E. R., Gantt, B.,
890 Anguelova, M. D., Bhave, P. V., Bird, J., Callaghan, A. H., Ceburnis, D., Chang, R., Clarke, A., de Leeuw,
891 G., Deane, G., DeMott, P. J., Elliot, S., Facchini, M. C., Fairall, C. W., Hawkins, L., Hu, Y., Hudson, J. G.,
892 Johnson, M. S., Kaku, K. C., Keene, W. C., Kieber, D. J., Long, M. S., Mårtensson, M., Modini, R. L.,
893 Osburn, C. L., Prather, K. A., Pszenny, A., Rinaldi, M., Russell, L. M., Salter, M., Sayer, A. M., Smirnov,
894 A., Suda, S. R., Toth, T. D., Worsnop, D. R., Wozniak, A., and Zorn, S. R.: Production mechanisms,
895 number concentration, size distribution, chemical composition, and optical properties of sea spray
896 aerosols, Atmospheric Science Letters, 14, 207-213, 10.1002/asl2.441, 2013.
897
898 Mikhailov, E., Vlasenko, S., Niessner, R., and Pöschl, U.: Interaction of aerosol particles composed of
899 protein and salts with water vapor: hygroscopic growth and microstructural rearrangement, Atmos. Chem.
900 Phys., 4, 323-350, 10.5194/acp-4-323-2004, 2004.
901
902 Mikhailov, E., Vlasenko, S., Martin, S. T., Koop, T., and Pöschl, U.: Amorphous and crystalline aerosol
903 particles interacting with water vapor: conceptual framework and experimental evidence for restructuring,
904 phase transitions and kinetic limitations, Atmos. Chem. Phys., 9, 9491-9522, 10.5194/acp-9-9491-2009,
905 2009.

906
907 Musick, J., Popp, J., and Kiefer, W.: Raman spectroscopic and elastic light scattering investigations of
908 chemical reactions in single electrodynamically levitated microparticles, Journal of Molecular Structure,
909 480–481, 317-321, http://dx.doi.org/10.1016/S0022-2860(98)00705-4, 1999.
910
911 Niedermeier, D., Wex, H., Voigtländer, J., Stratmann, F., Brüggemann, E., Kiselev, A., Henk, H., and
912 Heintzenberg, J.: LACIS-measurements and parameterization of sea-salt particle hygroscopic growth and
913 activation, Atmos. Chem. Phys., 8, 579-590, 10.5194/acp-8-579-2008, 2008.
914
915 Pant, A., Parsons, M. T., and Bertram, A. K.: Crystallization of Aqueous Ammonium Sulfate Particles
916 Internally Mixed with Soot and Kaolinite: Crystallization Relative Humidities and Nucleation Rates, J.
917 Phys. Chem. A, 110, 8701-8709, doi: 10.1021/jp060985s, 2006.
918
919 Park, K., Kim, J.-S., and Miller, A.: A study on effects of size and structure on hygroscopicity of
920 nanoparticles using a tandem differential mobility analyzer and TEM, J. Nanopart. Res., 11, 175-183,
921 10.1007/s11051-008-9462-4, 2009.
922
923 Pöhlker, C., Saturno, J., Krüger, M. L., Förster, J.-D., Weigand, M., Wiedemann, K. T., Bechtel, M.,
924 Artaxo, P., and Andreae, M. O.: Efflorescence upon humidification? X-ray microspectroscopic in situ
925 observation of changes in aerosol microstructure and phase state upon hydration, Geophys. Res. Lett., 41,
926 2014GL059409, 10.1002/2014gl059409, 2014.
927
928 Prather, K. A., Bertram, T. H., Grassian, V. H., Deane, G. B., Stokes, M. D., DeMott, P. J., Aluwihare, L. I.,
929 Palenik, B. P., Azam, F., Seinfeld, J. H., Moffet, R. C., Molina, M. J., Cappa, C. D., Geiger, F. M., Roberts,
930 G. C., Russell, L. M., Ault, A. P., Baltrusaitis, J., Collins, D. B., Corrigan, C. E., Cuadra-Rodriguez, L. A.,
931 Ebben, C. J., Forestieri, S. D., Guasco, T. L., Hersey, S. P., Kim, M. J., Lambert, W. F., Modini, R. L., Mui,
932 W., Pedler, B. E., Ruppel, M. J., Ryder, O. S., Schoepp, N. G., Sullivan, R. C., and Zhao, D.: Bringing the
933 ocean into the laboratory to probe the chemical complexity of sea spray aerosol, Proc. Natl. Acad. Sci.,
934 110, 7550-7555, 10.1073/pnas.1300262110, 2013.
935
936 Saul, T. D., Tolocka, M. P., and Johnston, M. V.: Reactive Uptake of Nitric Acid onto Sodium Chloride
937 Aerosols Across a Wide Range of Relative Humidities, J. Phys. Chem. A, 110, 7614-7620,
938 10.1021/jp060639a, 2006.
939
940 Schindelholz, E., Risteen, B. E., and Kelly, R. G.: Effect of Relative Humidity on Corrosion of Steel under
941 Sea Salt Aerosol Proxies: II. MgCl2, Artificial Seawater, J. Electrochem. Soc., 161, C460-C470,
942 10.1149/2.0231410jes, 2014.
943
944 Schlenker, J. C., and Martin, S. T.: Crystallization Pathways of Sulfate−Nitrate−Ammonium Aerosol
945 Particles, J. Phys. Chem. A, 109, 9980-9985, 10.1021/jp052973x, 2005.
946
947 Seidell, A., and Linke, W. F.: Solubilities of Inorganic and Metal Organic Compounds, 4th ed., American
948 Chemical Society, Washington, DC., 1965.
949
950 Seinfeld, J. H., and Pandis, S. N.: Atmospheric chemistry and physics : from air pollution to climate
951 change, 2nd ed., J. Wiley & Sons Inc., Hoboken, N.J., 2006.
952
953 Tang, I. N.: Phase transformation and growth of aerosol particles composed of mixed salts, J. Aerosol Sci.,
954 7, 361-371, http://dx.doi.org/10.1016/0021-8502(76)90022-7, 1976.
955

956 Tang, I. N., Tridico, A. C., and Fung, K. H.: Thermodynamic and optical properties of sea salt aerosols, J.
957 Geophys. Res. — Atmos., 102, 23269-23275, 10.1029/97jd01806, 1997.

958
959 ten Brink, H. M.: Reactive uptake of HNO3 and H2SO4 in sea-salt (NaCl) particles, J. Aerosol Sci., 29,
960 57-64, http://dx.doi.org/10.1016/S0021-8502(97)00460-6, 1998.

961
962 Wang, P., Pitzer, K. S., and Simonson, J. M.: Thermodynamic Properties of Aqueous Magnesium Chloride
963 Solutions From 250 to 600 K and to 100 MPa, J. Phys. Chem. Ref. Data., 27, 971-991,
964 doi:http://dx.doi.org/10.1063/1.556026, 1998.

965
966 Wexler, A. S., and Seinfeld, J. H.: Second-generation inorganic aerosol model, Atmos. Environ., 27A, 25,
967 2731-2748, http://dx.doi.org/10.1016/0960-1686(91)90203-J, 1991.

968
969 Wexler, A. S., and Clegg, S. L.: Atmospheric aerosol models for systems including the ions H+, NH4+,
970 Na+, SO42−, NO3−, Cl−, Br−, and H2O, J. Geophys. Res. — Atmos., 107, ACH 14-11-ACH 14-14,
971 10.1029/2001jd000451, 2002.

972
973 Wise, M. E., Semeniuk, T. A., Bruintjes, R., Martin, S. T., Russell, L. M., and Buseck, P. R.: Hygroscopic
974 behavior of NaCl-bearing natural aerosol particles using environmental transmission electron microscopy,
975 J. Geophys. Res. — Atmos., 112, D10224, 10.1029/2006jd007678, 2007.

976
977 Wise, M. E., Freney, E. J., Tyree, C. A., Allen, J. O., Martin, S. T., Russell, L. M., and Buseck, P. R.:
978 Hygroscopic behavior and liquid-layer composition of aerosol particles generated from natural and
979 artificial seawater, J. Geophys. Res. — Atmos., 114, D03201, 10.1029/2008jd010449, 2009.

980
981 Woods, E., Chung, D., Lanney, H. M., and Ashwell, B. A.: Surface Morphology and Phase Transitions in
982 Mixed NaCl/MgSO4 Aerosol Particles, J. Phys. Chem. A, 114, 2837-2844, 10.1021/jp911133j, 2010.

983
984 Woods, E., Yi, C., Gerson, J. R., and Zaman, R. A.: Uptake of Pyrene by NaCl, NaNO3, and MgCl2
985 Aerosol Particles, J. Phys. Chem. A, 116, 4137-4143, 10.1021/jp3014145, 2012.

986
987 Xiao, H.-S., Dong, J.-L., Wang, L.-Y., Zhao, L.-J., Wang, F., and Zhang, Y.-H.: Spatially Resolved Micro-
988 Raman Observation on the Phase Separation of Effloresced Sea Salt Droplets, Environ. Sci. Technol., 42,
989 8698-8702, 10.1021/es801181f, 2008.

990
991 Zuend, A., Marcolli, C., Luo, B. P., and Peter, T.: A thermodynamic model of mixed organic-inorganic
992 aerosols to predict activity coefficients, Atmos. Chem. Phys., 8, 4559-4593, 10.5194/acp-8-4559-2008,
993 2008.

994
995 Zuend, A., Marcolli, C., Booth, A. M., Lienhard, D. M., Soonsin, V., Krieger, U. K., Topping, D. O.,
996 McFiggans, G., Peter, T., and Seinfeld, J. H.: New and extended parameterization of the thermodynamic
997 model AIOMFAC: calculation of activity coefficients for organic-inorganic mixtures containing carboxyl,
998 hydroxyl, carbonyl, ether, ester, alkenyl, alkyl, and aromatic functional groups, Atmos. Chem. Phys., 11,
999 9155-9206, 10.5194/acp-11-9155-2011, 2011.

1000

1001

Table 1. Encountering frequencies (in %) of Types A, B, and C particles, showing different mutual deliquescence behavior (details in text), at various mixing ratios of NaCl–MgCl$_2$.

Mole fraction of NaCl (X_{NaCl})	Encountering frequencies (in %)		
	Type A particles	Type B particles	Type C particles
0.01	94	6	-
0.026	94	6	-
0.05	96	4	-
0.1	24	29	47
0.2	36	45	18
$0.3 \leq X_{NaCl} \leq 0.9$	100	-	-

Figure 1. Plot of 2-D area ratio (A/A_0) of nebulized pure (a) NaCl and (b) MgCl$_2$ as a function of the RH. The recorded transition RHs in both humidification and dehydration processes are marked with arrows.
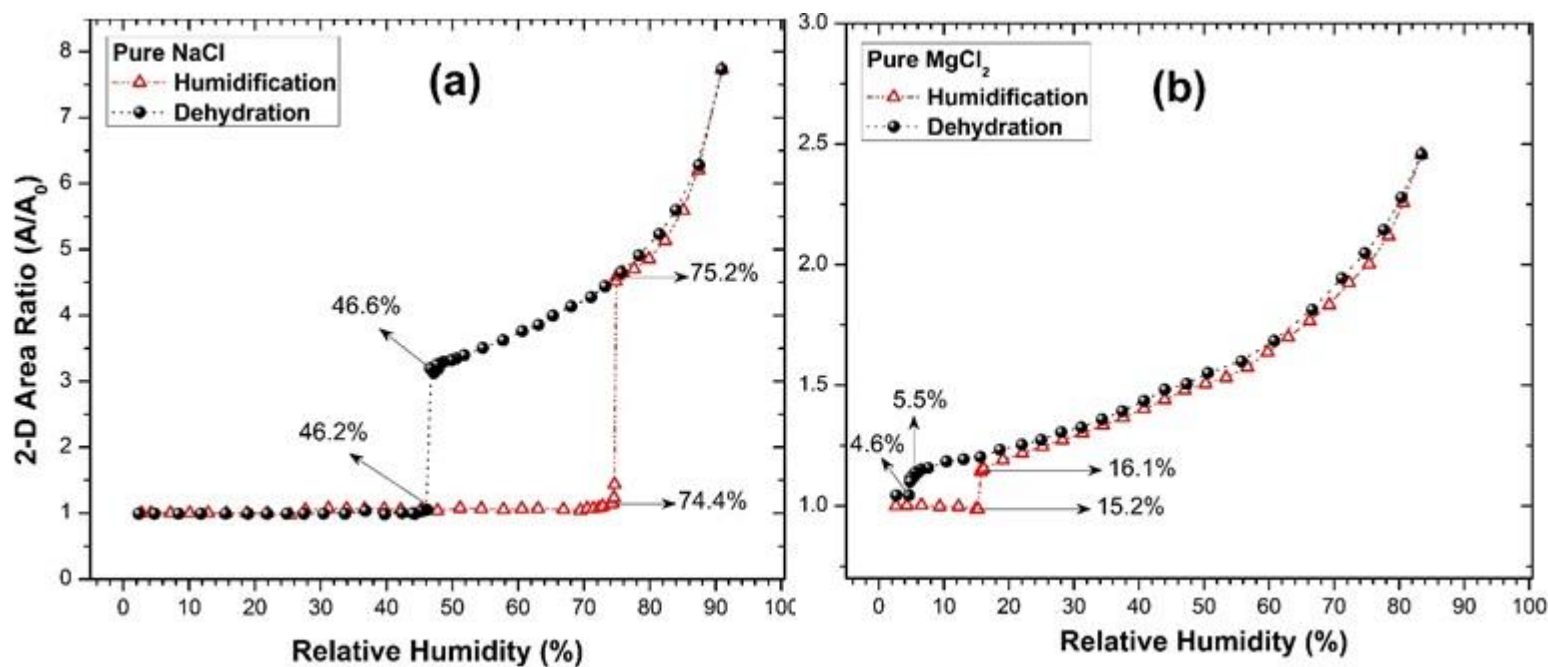
Figure 2. Optical images and corresponding Raman spectra obtained by in-situ RMS, for a representative dry-deposited $MgCl_2 \cdot 6H_2O$ particle during (a) humidification (1st cycle), (b) dehydration (1st cycle), and (c) humidification (2nd cycle) processes and for a representative wet-deposited $MgCl_2$ particle during (d) humidification and (e) dehydration processes.
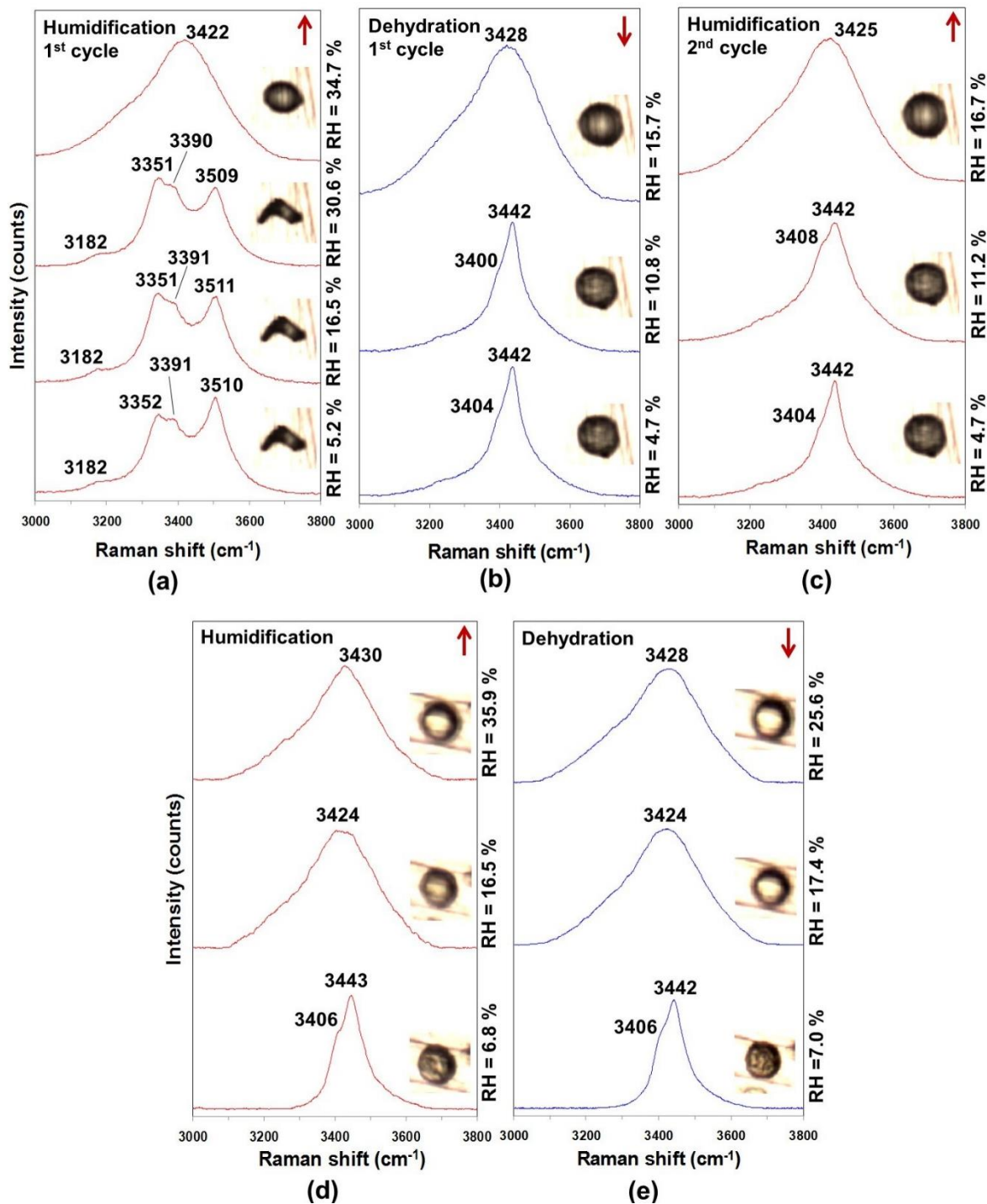
Figure 3. Plot of 2-D area ratio (A/A_0) of a NaCl-rich particle with a seawater-like mixing ratio of $X_{NaCl} = 0.9$ as a function of RH. The recorded optical images of the particle/droplet along with transition RHs in both humidification and dehydration processes are marked with arrows.
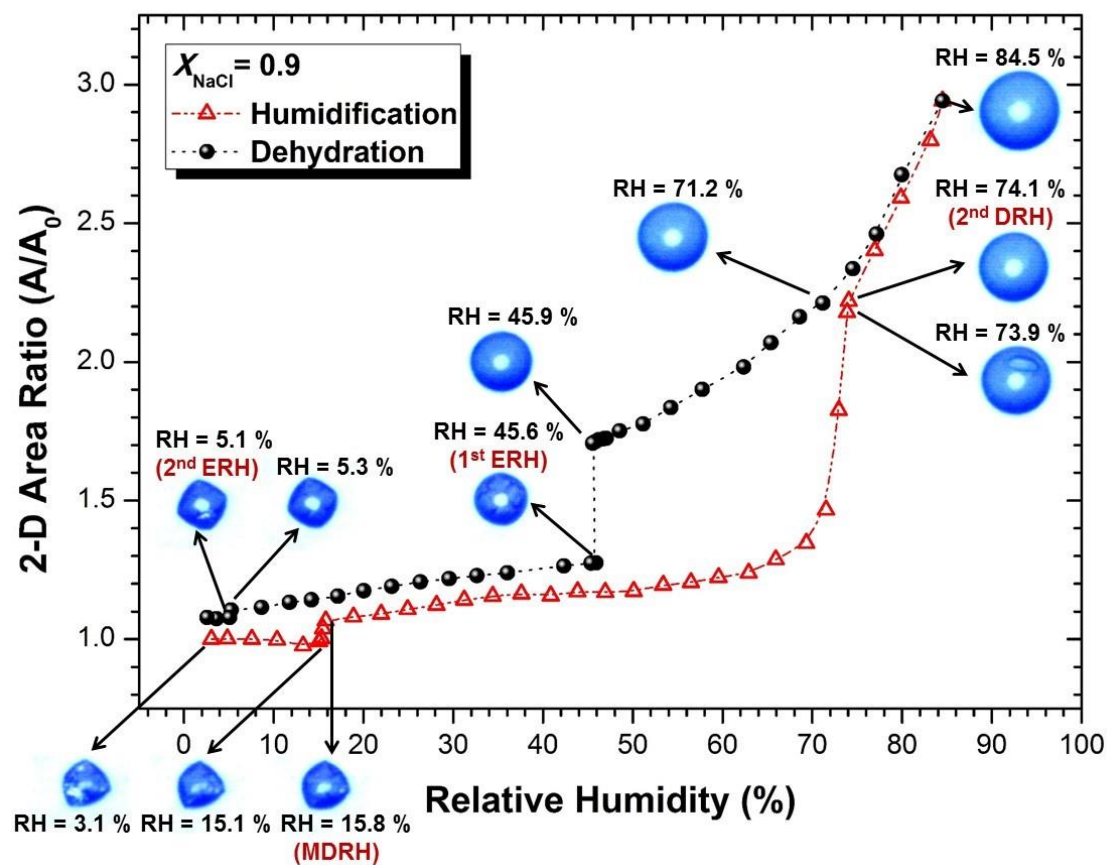
Figure 4. Plots of 2-D area ratio (A/A_0) of NaCl–MgCl$_2$ mixture aerosol particles with (a) NaCl-rich mixing ratio of $X_{NaCl} = 0.5$; (b) MgCl$_2$-dominant eutonic composition of $X_{NaCl} = 0.026$; and (c) MgCl$_2$-dominant mixing ratio of $X_{NaCl} = 0.01$ as a function of RH. The recorded transition relative humidities in both humidification and dehydration processes are marked with arrows.
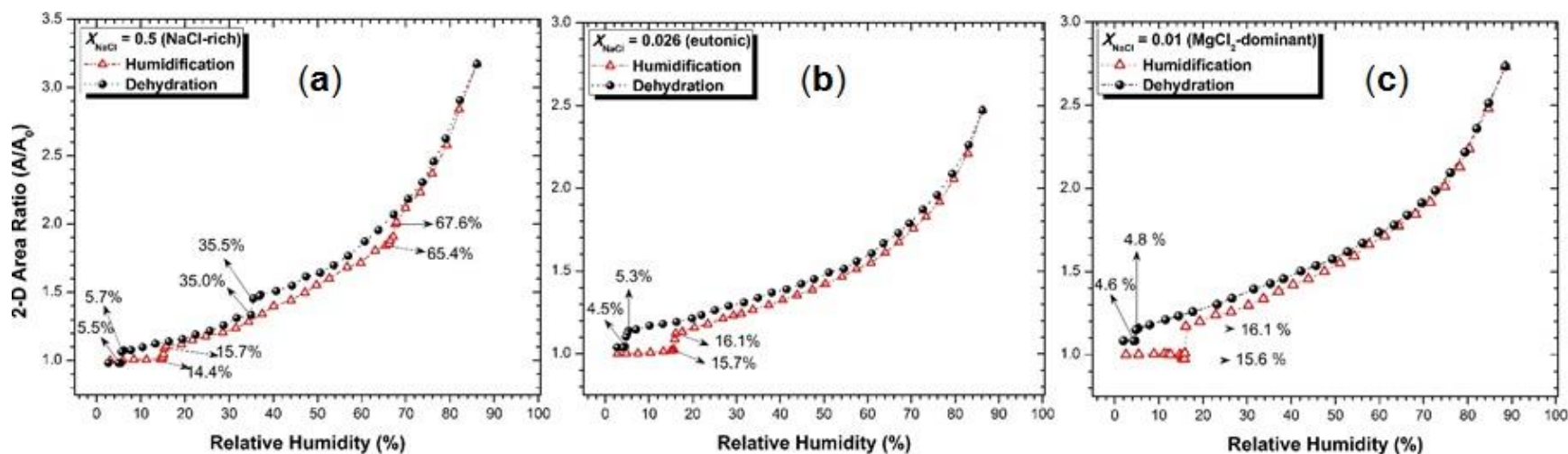
Figure 5. Plots of the 2-D area ratio (A/A_0) of three representative particles with a composition of X_{NaCl} = 0.2, showing different deliquescence behaviors during the humidification process, as a function of RH. During the humidification process, (a) "Type A" particle shows two deliquescence transitions with MDRH of 15.8 %, (b) "Type B" particle shows three deliquescence transitions as well as one efflorescence transition, and (c) "Type C" particle shows two deliquescence transitions with MDRH of 33.0 %. During the dehydration process, Types A and B particles show the second ERH of 5.2 %, whereas the Type C particle shows a second ERH of 23.7 %. The recorded optical images of the particles/droplets along with the transition RHs during both humidification and dehydration processes are marked with arrows.
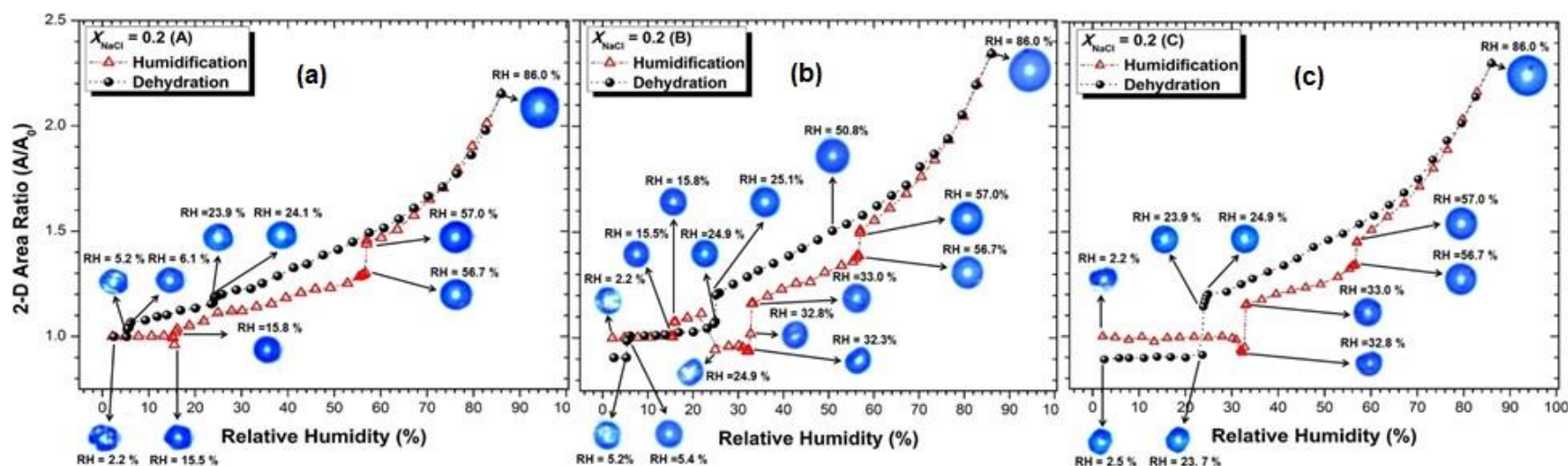
Figure 6. Characteristic OH-stretching Raman spectra and corresponding optical images of NaCl-MgCl₂ mixture particles with a composition of $X_{NaCl} = 0.2$, recorded by in-situ RMS. Three types of particles showing different hygroscopic behavior are shown. See the text for a detailed explanation.
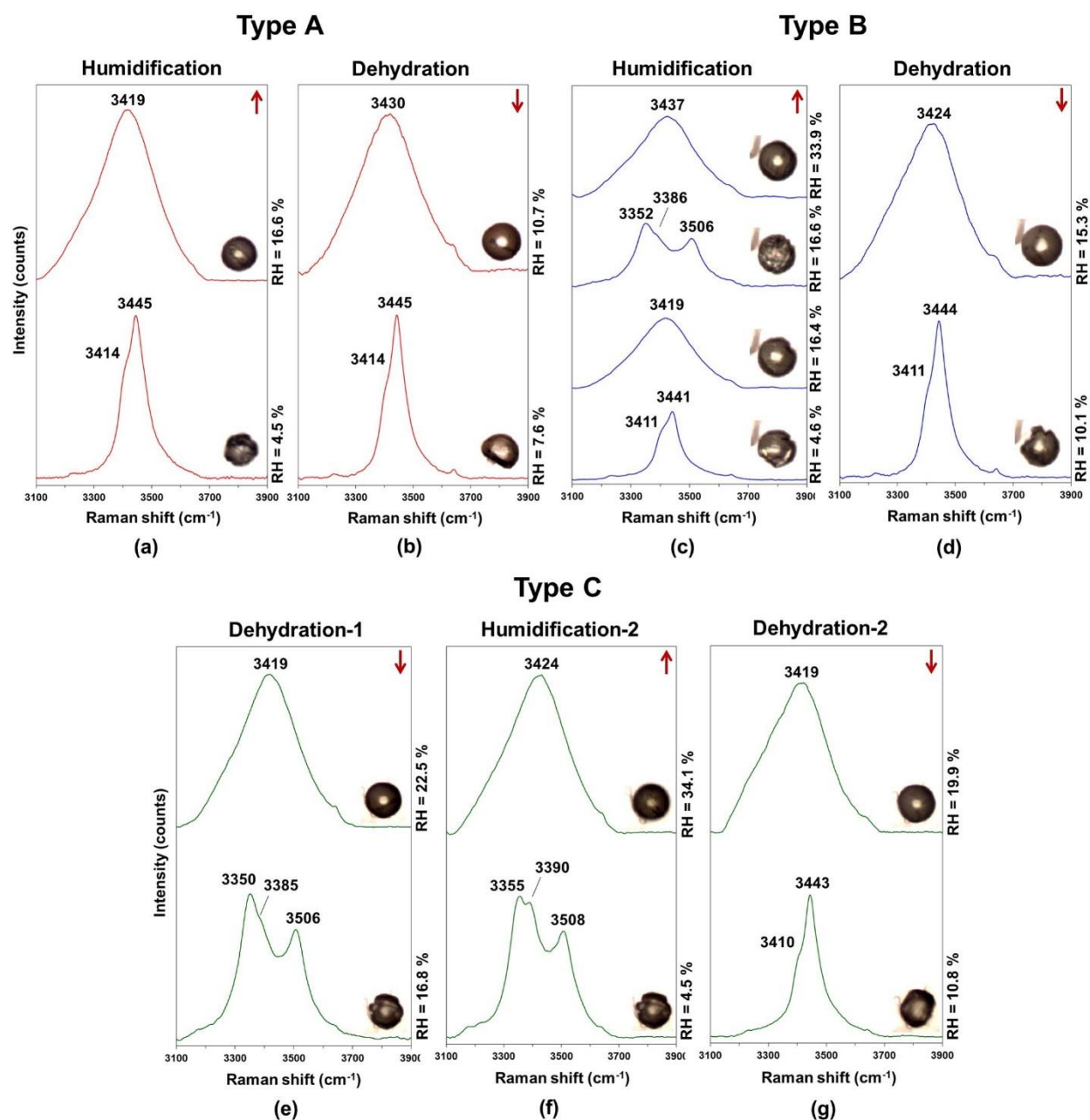
Figure 7. Measured MDRHs (MDRH$_1$ = 15.9 (±0.3) % ⇒ open blue triangles; MDRH$_2$ = 33.0 (±0.3) % ⇒ open brown circles) and the second DRH (closed black circles) and calculated MDRH (dotted red line) and the second DRHs (dash-dotted black curve) from the AIOMFAC, plotted as a function of the mole fraction of NaCl in NaCl-MgCl$_2$ mixture particles. The phase notations shown in brackets are: s = solid; and aq = aqueous. The brown shaded portion is where particles with three types of transitions (Types A, B, and C as in text) were observed for X_{NaCl} = 0.1 and 0.2. The dense and light brown shaded patterns indicate the high and low encountering frequencies of Types B and C particles, respectively. The average and range of ERHs observed during the humidification process for Type B particles are represented by purple stars and bars, respectively.
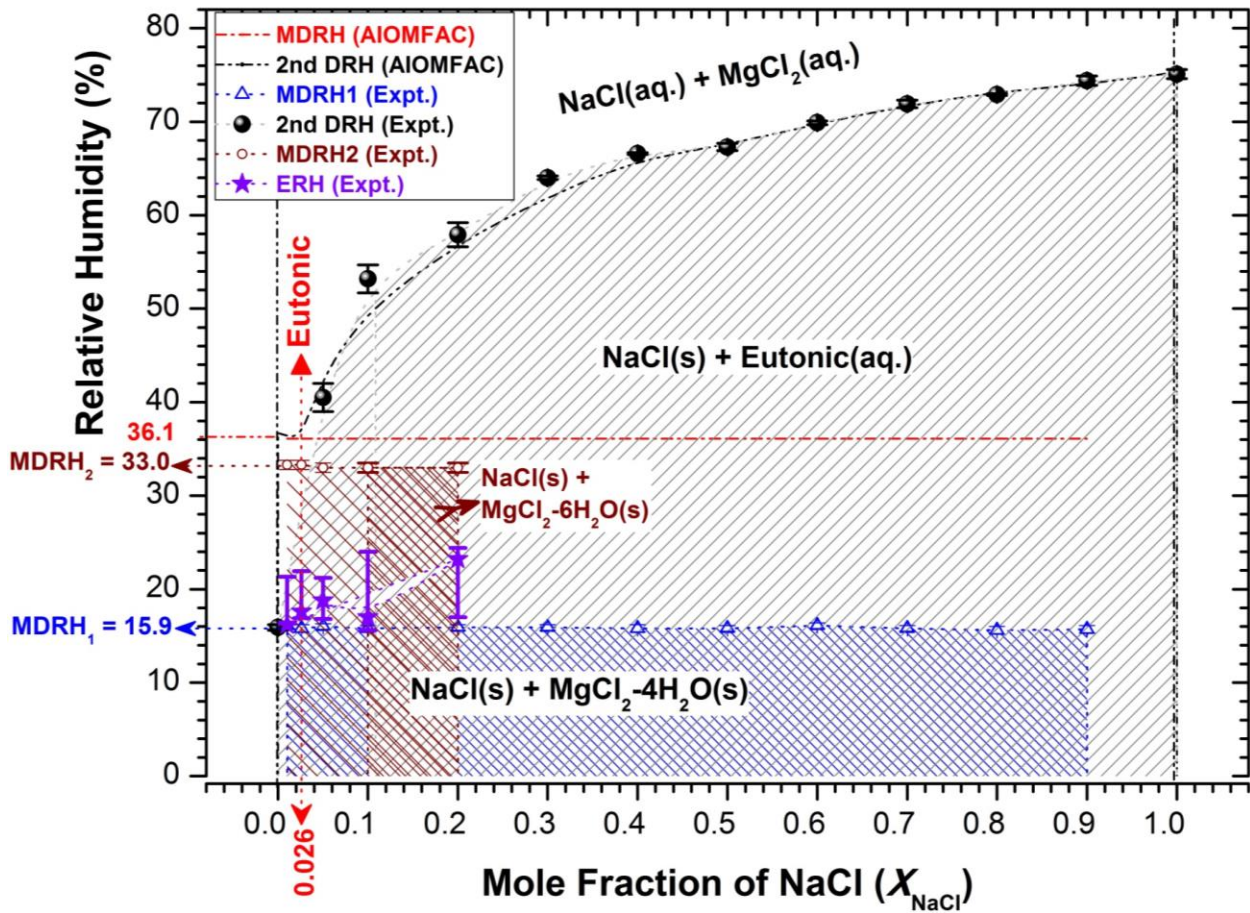
Figure 8. Measured first ERH values (closed black circles) and second ERH values (open blue triangles (MERH$_1$ for MgCl$_2$·4H$_2$O crystallization in Types A or B particles) and open purple stars (MERH$_2$ for MgCl$_2$·6H$_2$O crystallization in Type C particles)) as a function of the mole fraction of NaCl in NaCl-MgCl$_2$ mixture particles. The phase notations shown in brackets are s = solid; and aq = aqueous.
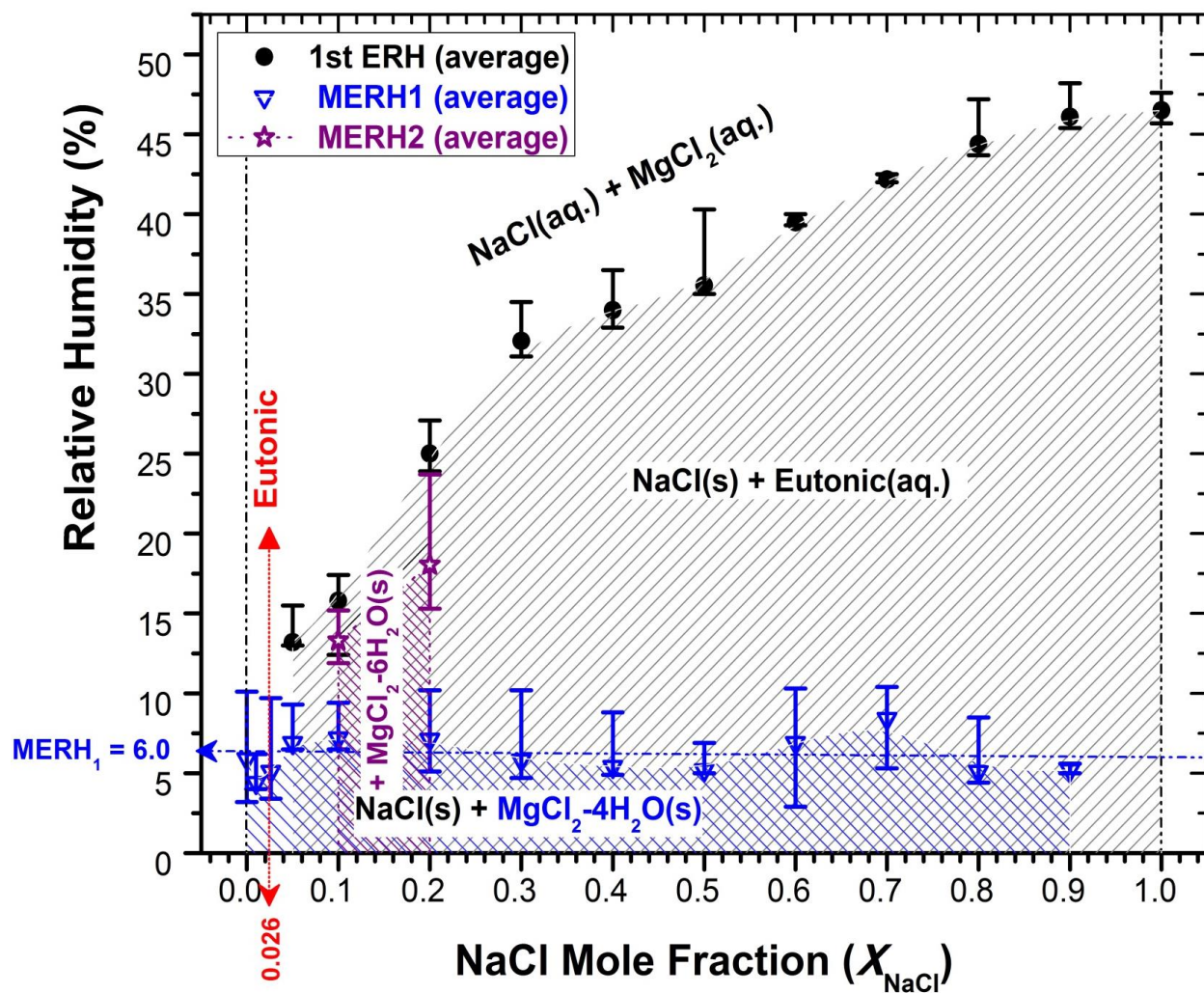
Figure 9. Elemental X-ray maps for Na (from NaCl), Mg (from $MgCl_2$), O (from $MgCl_2 \cdot xH_2O$), and mixed Na/Mg and secondary electron images (SEIs) of the effloresced NaCl-$MgCl_2$ mixture particles with compositions of (A) $X_{NaCl} = 0.9$ (NaCl-rich, seawater-like mixing ratio) and (B) $X_{NaCl} = 0.6$.